# Laser Spectroscopy Of Neutron-Deficient Bismuth Isotopes

Megan Jenkinson

MSc by Research

University Of York

Physics

September 2017

# Abstract

This thesis investigates the neutron-deficient isotopes $^{187,188,189,191}$Bi. A particular focus was placed on studying their alpha decay and isomeric states. The data analysed was gathered at the ISOLDE facility at CERN. Bi nuclei were produced through the collision of high energy protons with a uranium carbide target. A three-step laser ionisation process was used to extract two states of Bi: the ground state and an isomer. These were separately analysed. After mass separation, the Bi nuclei were implanted into carbon foils with silicon (Si) detectors used to measure alpha decays and high purity germanium (HPGe) detectors used to measure gamma decays.

The alpha decay schemes of the ground state and the isomeric state of Bi were derived from the Si energy spectra. By doing this, the hyperfine structure (HFS) was established and isotope shifts were deduced. Conclusions drawn from this research will assist in deducing the evolution of deformation of bismuth nuclei. This work is a collaborative extension of the experiments undertaken at Gatchina, Russia, as described in the latest publication by A. Barzakh et al [1]. Gatchina cannot access the lightest isotopes of Bi, hence, the work completed at ISOLDE is paramount in gaining a full understanding of Bi.

# Contents

# List of Figures

# List of Tables

I declare that this thesis is my own work and I am the sole author. This thesis has not been submitted prior to the date stated on the cover for an award at the University of York, or any other, institute. All sources are acknowledged and cited.

I would like to thank everyone at the University of York who has helped me throughout the course of my degree, notably, Professor Andrei Andreyev, James Cubiss, and Christopher Raison. The countless meetings we have had have been invaluable and have not gone unappreciated.

# Chapter 1

# Introduction

This chapter covers the key physics concepts, such as nuclear structure and decay processes, behind the experiment undertaken.

## 1.1 Nuclear Structure

Nuclei have been a topic of interest since their discovery in 1911 by the famous Ernest Rutherford scattering experiment. Rutherford hypothesised that positive charge was contained within a small region at the centre of the atom, the nucleus. Whilst nuclei are of the order of 10 fm in diameter, atoms are around five orders of magnitude larger. Within the nucleus exists the positively charged protons, and the neutral neutrons, collectively referred to as nucleons [2].

The elements of the periodic table have different numbers of protons hence, different numbers of electrons. For a neutral atom the number of electrons is equal to the numbers of protons, Z. The electron configuration of an atom is responsible for its chemical properties. Nuclei with differing numbers of neutrons, N, but, the same amount of protons, Z, are known as isotopes. An atom is characterised by its mass number, A, the total number of nucleons, A=N+Z [3].

Figure 1.1 shows the chart of nuclides. This chart shows the various methods of decay a specific nucleus may undergo. Alpha decay is an important process for this particular thesis and is later discussed in section 1.2.

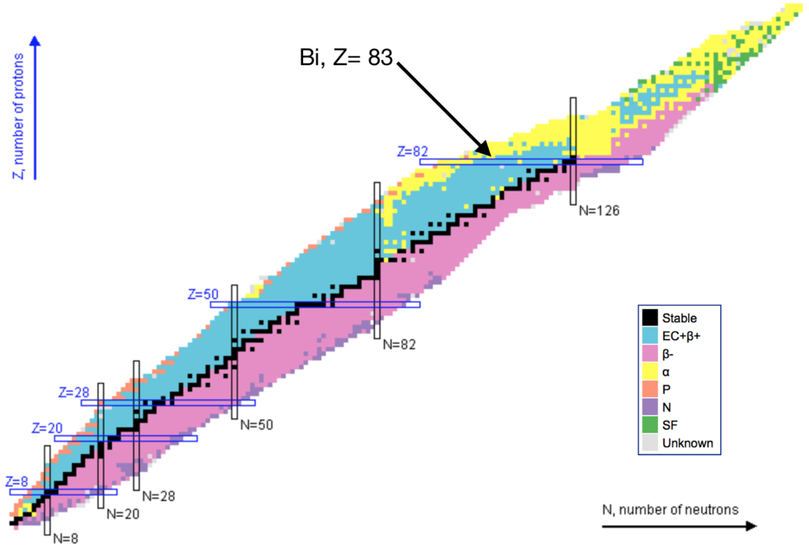

**Figure 1.1:** Chart of nuclides. The various decay modes are indicated by colour. The region of interest within this thesis is when Z=83. Figure taken from [4].

Similar to the electronic configuration of electrons in an atom, nucleons exist within a shell structure. Due to the Pauli exclusion principle, no two protons or neutrons can exist in the same state. Stability of the nucleus is affected by whether or not it has a closed shell. A closed shell only occurs at certain numbers of nucleons, commonly known as a magic number, when Z or N= 2, 8, 20, 28, 50 and 82. To explain the physics behind the magic numbers the Woods-Saxon potential can be utilised, a central field potential simulating a rounded square well. Refer to figure 1.2 for the shell model [5, 6].

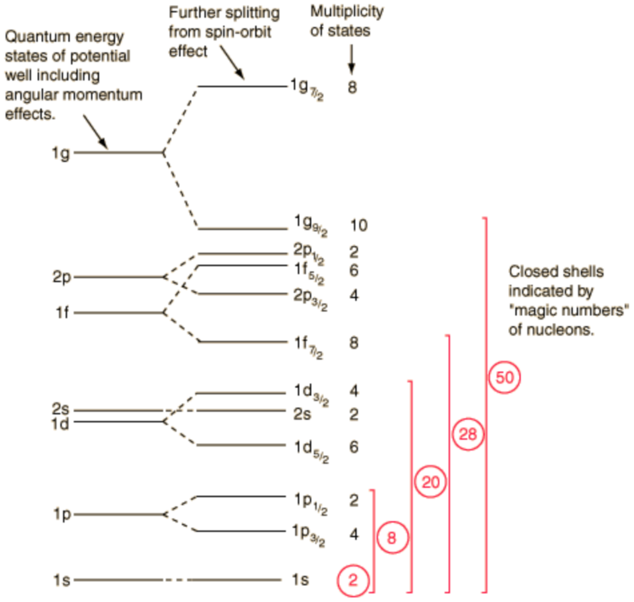

**Figure 1.2:** Shell model diagram, first five magic numbers shown. Figure taken from [7].

The lowest energy state of a nucleus is known as the ground state, yet isomeric states do exist. An isomeric state refers to a nuclide in an excited nuclear state, with a lifetime longer than a typical excited state, yet a different nucleon configuration in the ground state [8].

## 1.2 Nuclear Decay Processes

### 1.2.1 Alpha Decay

During alpha decay a helium nucleus is emitted from the parent. This occurs spontaneously and is represented by the following:

$$ {}^{\mathrm{A}}_{\mathrm{Z}}\mathrm{X}_{\mathrm{N}} \longrightarrow {}^{\mathrm{A-4}}_{\mathrm{Z-2}}\mathrm{X}'_{\mathrm{N-2}} \; + \; \alpha \tag{1.1} $$

where X is the parent nucleus and X' is the daughter [9]. The net energy liberated in the emission of an $\alpha$ particle from a nucleus of mass m(X) is the $Q_\alpha$ value, given by:

$$ Q_\alpha = (m(X) - m(X') - m(\alpha))c^2 \tag{1.2} $$

$\alpha$ decay is a two body problem therefore, $Q_\alpha$ can be calculated from the kinetic energy of the $\alpha$ particle ($T_\alpha$), see equation 1.3. In order for any decay to occur the reaction must have positive $Q$ value. Using the conservation of energy and momentum, and considering that $T_\alpha$ is typically $<$ 10 MeV, relativistic mechanics may be neglected [2].

$$ Q = T_\alpha(1 + \frac{m_\alpha}{m_{X'}}) \tag{1.3} $$

According to the semi-empirical mass equation, the emission of an $\alpha$ particle decreases the Coulomb energy of the nucleus hence, increases the stability of heavy nuclei. The He nucleus is tightly bound, as it is a doubly magic nucleus, therefore a high mass defect. Energies of the emitted alpha particles are known to increase with the atomic number of the parent [2, 10].

Due to an interplay of a nuclear potential and the Coulomb repulsion potential between the alpha particle and the daughter nucleus, a barrier emerges [2]. The alpha particle can leave the nucleus by tunnelling through this barrier. Without the Coulomb barrier the nucleus could freely alpha decay, as long as $Q_\alpha > 0$, the barrier provides a hindrance factor in turn increasing the lifetime of the parent nucleus [3]. Geiger and Nuttall came across the relationship between the alpha particle energy $Q_\alpha$ and the transition probability, T:

$$ logT = a + \frac{b}{\sqrt{Q_\alpha}} \tag{1.4} $$

Here **a** and **b** are constants, equations taken from [2]. As with other particles the alpha particle has an angular momentum assigned to it, due to the intrinsic spin of an alpha particle being zero, the angular momentum is purely orbital. Allowed values for the angular momentum of the alpha particle, $l_\alpha$, are:

$$|I_i - I_f| \leq l_\alpha \leq I_i + I_f \tag{1.5}$$

where $I_i$, is the angular momentum of the initial nuclear state and $I_f$, the final state. The selection rule is such that if the parity changes this is an odd transition, but if the initial and final state are of the same parity this is an even transition [2]. Parity of the He nucleus is given by: $(-1)^{l_\alpha}$. Due to the helium nucleus having both even numbers of neutrons and protons the parity will always be positive. The parity of any nucleus is defined by its angular momentum.

### 1.2.2 Beta Decay

The emission of an electron, commonly known as a $\beta$- particle, was one of the first forms of decay to be observed. Alternatively, electron capture was not observed until 1938. Positron emission or positive $\beta$ decay was discovered in 1934 by the Joliot-Curies, where a proton was converted to a neutron [2]. During $\beta^+$ and $\beta^-$ decay, an electron or positron is produced from the excess decay energy. Whereas electron capture involves the parent nucleus capturing an orbital electron along with the emission of a neutrino. A hole is now present in the orbital from which the captured electron came, hence, an electron from a higher orbital will drop down to fill this vacancy, accompanied by the emission of an X-ray [11]. The three decay processes are as follows:

$$\mathrm{n} \rightarrow \mathrm{p} + \mathrm{e}^- + \bar{\nu} \text{ (negative } \beta \text{ decay)}, \tag{1.6}$$

$$\mathrm{p} \rightarrow \mathrm{n} + \mathrm{e}^+ + \nu \text{ (postitive } \beta \text{ decay)}, \tag{1.7}$$

and

$$\mathrm{p} + \mathrm{e}^- \rightarrow \mathrm{n} + \nu \text{ (orbital electron capture}, \epsilon), \tag{1.8}$$

equations taken from [2]. Each of these decays are classed as a weak interaction, the quark flavour within the nucleon changes, whilst an electron or positron is produced/captured. During the above decays a neutrino or an anti-neutrino is also emitted in order to conserve energy and momentum. These particles carry no charge and have a spin of a $\frac{1}{2}$ [2].

Emitted electrons have a range of energies the maximum value being equal to the Q value and a minimum of zero. As in $\alpha$ decay the Q value of the reaction is equivalent to the difference between the initial and final nuclear mass energies [3].

$$Q_{\beta^-} = [m(^{\mathrm{A}}\mathrm{X}) - m(^{\mathrm{A}}\mathrm{X}')]c^2, \tag{1.9}$$

$$Q_{\beta^+} = [m(^{\mathrm{A}}\mathrm{X}) - m(^{\mathrm{A}}\mathrm{X}') - 2m_e]c^2, \tag{1.10}$$

$$Q_{\epsilon} = [m(^{\mathrm{A}}\mathrm{X}) - m(^{\mathrm{A}}\mathrm{X}')]c^2 - E_B. \tag{1.11}$$

Where $m^A(X)$ refers to the atomic mass and $m_e$, the electron mass [9].

### 1.2.3 Gamma Decay and Internal Conversion

Gamma decay, $\gamma$, is when a nucleus in an excited state releases excess energy in the form of a photon. During this process there is no change in mass or proton number, only energy is expelled from the system. Gamma-ray transitions are not always required to decay to the ground state. The energy of the released photon corresponds to the energy difference between the initial and final state. Multiple decays can occur in order to reach the ground state, leading to a cascade of $\gamma$ rays, unique to each nucleus [12].

Both magnetic and electrical fields are present within the nucleus. This is due to the orbital motion of the nucleons along with their individual spins, which leads to oscillating electric currents and electric charges. Resulting $\gamma$ rays from the magnetic field, are assigned, ML, for magnetic multipole radiation. $\gamma$ rays from the electric field, are assigned, EL, for electric multipole radiation. The resulting radiation can further be categorised depending on whether it is a product of dipole, quadrupole or multipole expansion. Hence gamma rays can be classed as an E1, for an electric dipole, E2, electric quadrupole radiation, M1, magnetic dipole or M2, for a magnetic quadrupole radiation. Octupole and hexadecapole radiation also exists, L=3 and L=4 [12].

Angular momentum and parity($\pi$) must be conserved, as in alpha decay. Refer to equation 1.5 for the allowed values of the emitted photon. In the case of parity of the radiation field, in order to have an even parity the initial and final states must be equal. A field with odd parity will change the parity of the nucleus. The parity does not change for electric transitions with an even L, or magnetic transitions with an odd L. Electric transitions with an odd L, will change the parity, this applies to magnetic transitions with an even L [2, 12].

$$\Delta\pi = no : M1, E2, M3, E4..... \tag{1.12}$$

$$\Delta\pi = yes : E1, M2, E3, M4.... \tag{1.13}$$

Competing with gamma decay is internal conversion, an electromagnetic process. Internal conversion does not result in the emission of a photon, instead the electromagnetic multipole fields interact with the atomic electrons causing one to be released from the atom. Unlike beta decay the electron already exists within the atom and is then expelled. The transition energy $\Delta E$ is equal to the kinetic energy of the emitted electron plus the binding energy that is provided to release the electron from its atomic shell. Emitted electrons are labelled according to the electronic shell they originated from: K, L, M...

Electrons released in this process leave behind a vacancy in their atomic shell, this must be filled by an electron from a shell of higher energy. The resultant transitions lead to photon (X-Ray) emission. The energy of the resulting X-Rays is equivalent to the difference in shell energies, which can be detected in the $\gamma$ ray spectrum [9].

To characterise total internal conversion and its competition with gamma decay, it is useful to define the internal conversion coefficient $\alpha_{ic}$:

$$\alpha_{ic} = \frac{\lambda_e}{\lambda_\gamma}, \tag{1.14}$$

where $\lambda_e$ is equal to the sum of the probabilities of internal conversion of each electron shell, and $\lambda_\gamma$ is the probability of the transition occurring via $\gamma$ decay [2].

## 1.3 Hyperfine Structure

Hyperfine structure occurs due to the coupling between the electronic ($\mathbf{J}$) and nuclear ($\mathbf{I}$) angular momenta. This results in a change in the energy levels of the electrons and is termed the HFS [2, 13]. The total angular momentum ($\mathbf{F}$) is given by:

$$\mathbf{F} = \mathbf{I} + \mathbf{J} \tag{1.15}$$

The coupling of ($\mathbf{I}$) and ($\mathbf{J}$) angular momenta produces multiple values of ($\mathbf{F}$) :

$$|\mathbf{I} - \mathbf{J}| \leq \mathbf{F} \leq \mathbf{I} + \mathbf{J} \tag{1.16}$$

Consequently there are 2**J**+1 allowed values of **F** for a given transition (if $\mathbf{J} > \mathbf{I}$ there are 2**I**+1 allowed values). In this experiment lasers were utilised to measure the hyperfine splitting of Bi isotopes.

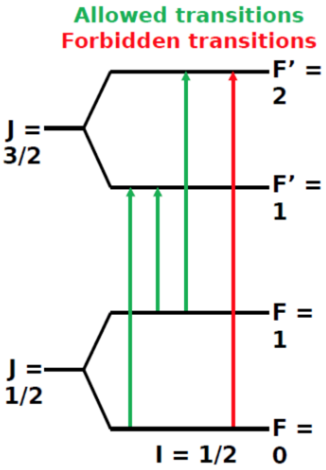

**Figure 1.3:** A diagram of the HFS of two different energy levels, both with I=1/2 and electron spins J=1/2 and 3/2. F is the product of I and J, as seen in equation 1.15. The allowed transitions are labelled, equation 1.20 enables all the allowed transitions to be found.

Figure 1.3 shows the splitting of two energy levels for a particular atom. The energy difference between each of the levels is given by:

$$\Delta E/h = \frac{K}{2}A + \frac{3K(K+1) - 4I(I+1)J(J+1)}{8I(2I-1)J(2J-1)}B \tag{1.17}$$

equation taken from [13]. Hyperfine parameters are A and B, and K=F(F+1)-I(I+1)-J(J+1), where

$$A = \frac{\mu_I B_e(0)}{IJ} \tag{1.18}$$

and

$$B = eQ_s\left\langle \frac{\delta^2 V_0}{\delta Z^2} \right\rangle. \tag{1.19}$$

The first term arises from the interaction between the magnetic moment of the nucleus and the magnetic field produced by the electrons at the site of the nucleus. The second term arises from the interaction between the electric quadrupole moment of the nucleus and the electric field gradient produced by the electrons [13]. Only certain transitions between energy levels are allowed, this is given by:

$$\Delta F = 0, \pm 1. \tag{1.20}$$

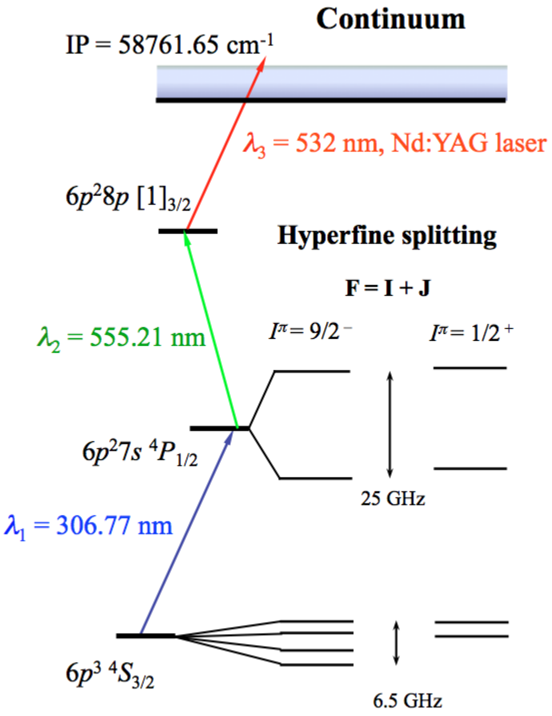

**Figure 1.4:** $^{191}$Bi HFS splitting in both the ground and an isomeric state. Vertical black lines between the energy levels represent allowed transitions. Distance between the energy levels shown in GHz.

From figure 1.4 it is clear that there are only three allowed transitions for the isomer state and six allowed transitions for the ground state in $^{191}$Bi. The transitions from the isomer state produced the HFS plot seen in figure 1.5.

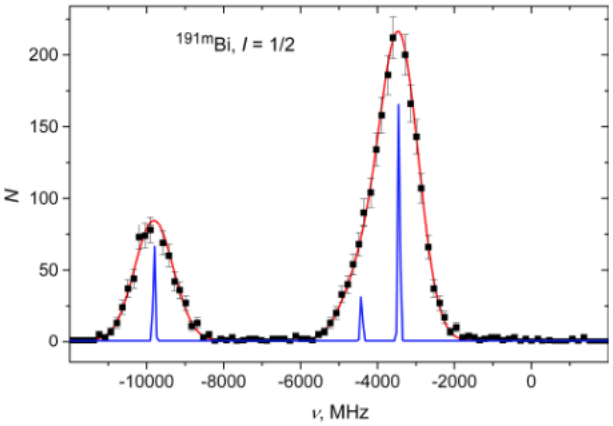

**Figure 1.5:** HFS plot for the isomer state of $^{191}$Bi. The blue lines represent the expected peaks to be seen, the black dots are the actual data points which have been fitted in red.

The HFS plot in figure 1.5 shows two large peaks within which are three smaller peaks. From Doppler broadening of the line width due to the thermal motion of atoms, only two peaks can be seen (the larger peaks fitted in red). Theoretically three peaks should be visible as there are three allowed transitions. The separation between the two large peaks seen, 15 GHz, is equivalent to the difference between F'=0 and F'=1 levels in the intermediate electronic state.

In the ground state, I=9/2, there are six possible transitions, which correspond to figure 1.6.

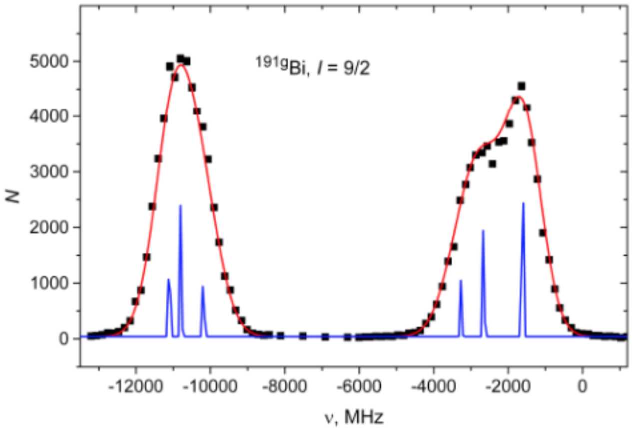

**Figure 1.6:** HFS plot for the ground state of $^{191}$Bi. Blue lines represent the expected peaks to be seen, data points (black) which have been fitted (red).

Once again six peaks should be visible within this plot yet only two are present. By exploiting laser spectroscopy to analyse the HFS of different states of Bi, the magnetic moment and spins were established. Isomeric states were determined from the shifting of spectral lines due to HFS. The transition frequency, $\nu$, also known as the centroid, is equal to the difference between the centre's of gravity of each HFS peak. However HFS does not alter the centre of gravity in first order perturbation theory [13].

## 1.4 Isotope shift

The frequency of the same atomic transition is seen to change between isotopes of the same element. This effect is known as isotope shift (IS). There are two factors that contribute to the isotope shift. The mass difference, which induces a change in the reduced electronic mass and the volume difference, which disrupts the electric charge distribution of the nucleus. IS occurs in all nuclei, shift is proportional to charge radius [14, 15]. This shift can be written as:

$$\delta\nu_{is}^{AA'} = \delta\nu_{ms}^{AA'} + \delta\nu_{fs}^{AA'} \tag{1.21}$$

this is a summation of field and mass shift, the mass shift is a result of the recoil of the nucleus. Mass shift consists of two components, the Normal Mass Shift which is equal to the Bohr reduced mass correction and the Specific Mass Shift is a result of the electron-electron correlations in a multi-electron system. The mass shift is given by:

$$\delta\nu^{AA'}_{mass\ shift} = \frac{m^{A'} - m^{A}}{m^{A} m^{A'}}(N + S) \tag{1.22}$$

where N and S are constants. Field shift arises as the energy of an atomic level is dependent on the size and shape of the electric charge distribution of the nucleus. Refer to figure 1.7 to see how the field shift varies from one isotope to the next. Isotopes of the same element have equal numbers of protons, but a different distribution of protons in space. The charge distribution is affected by the amount of neutrons within the nucleus. The nuclear charge distribution gives an electric field which defines the energy of the electrons. So, the field shift is the change in energy of a level as a result of a difference in this field between isotopes [16]. Field shift is given by:

$$\delta\nu^{AA'}_{field\ shift} = F\delta\langle r^2\rangle^{AA'} \tag{1.23}$$

F is an atomic factor. In even-even nuclei, the angular momentum caused by the nucleus is zero hence F=J, so:

$$\delta\nu^{AA'} = \nu^{A'} - \nu^{A} \tag{1.24}$$

where A and A' are the mass numbers of the isotopes in question.

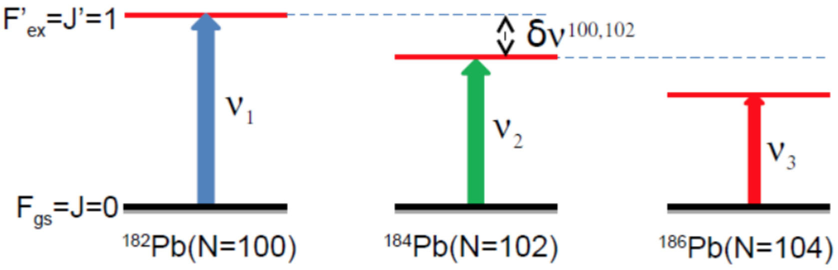

**Figure 1.7:** Schematic to demonstrate how the field shift $\delta\nu^{AA}$ changes amongst even-even lead isotopes.

Calculations carried out by Bodmer [17] confirm the theory that field shift is dependent on the mean-square charge radius [13].

# Chapter 2

# Motivation

This thesis focuses on the neutron-deficient isotopes of Bi namely: $^{187,188,189,191}$Bi. The purpose of such research is to develop understanding of shape coexistence, a spectacle displayed by various nuclei that can exist at a number of close lying energy minima, each presenting a unique type of deformation.

Most nuclei are deformed, however $^{16}$O, $^{40}$Ca and $^{208}$Pb are known to be spherical in their ground states. These particular nuclei are doubly magic. Constant deformation in the ground state of certain nuclei can occur by increasing the number of valence nucleons above a closed shell. The whole concept of shape coexistence stems from the fact that both the deformed and spherical shape of the nucleus can exist together at low excitation energies. Shape coexistence initially came to light in 1956 in a paper by Morinaga [18]. The paper focused on deformation of excited states of the nucleus in $^{16}$O. In 1972, isotopic shifts in mercury were measured at the ISOLDE facility at CERN using optical spectroscopy. The isotopic shifts for the lighter isotopes demonstrated shape staggering unlike the heavier isotopes. This suggested a large increase in the effective nuclear volume of Hg from N=107 to N=105 [19]. Seven years later nuclear shape isomerism was discovered in $^{185}$Hg via laser spectroscopy at ISOLDE. Due to shape coexistence a considerably large isomer shift was observed. Within $^{185}$Hg both oblate and prolate shapes are present. Refer to figure 2.1 for a representation of the nuclear deformation amongst nuclei as the neutron number decreases. Previous studies have demonstrated that the heavier isotopes, starting at $^{186}$Hg onwards are nearly spherical as N=126 shell approaches closure.

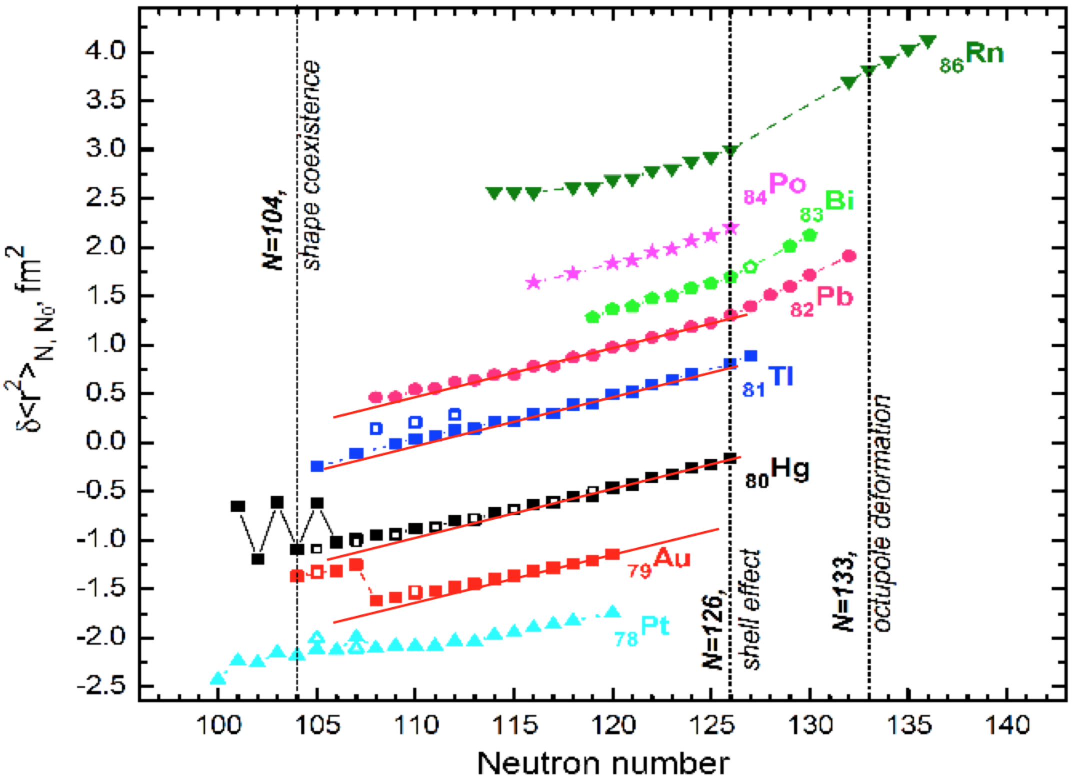

**Figure 2.1:** Plot demonstrating the deviations in rms of the nuclear charge radii of elements close to the lead region with differing numbers of neutrons. Plot provided by A. Andreyev, the data has been used in various papers but this particular plot has not been published [20].

From the liquid drop model it is known that the radius of the nucleus is proportional to $A^{1/3}$. Prior work has confirmed that heavier gold isotopes are almost spherical, this trend can be seen in figure 2.1 from $^{187}$Au to $^{199}$Au. Once $^{186}$Au is reached the nuclei become strongly deformed as neutrons are removed. Many Au isotopes follow the liquid drop model, the heavier isotopes decrease in radius as the neutron number decreases. It is only in the region of N≤107 when the nuclei experience deformation.

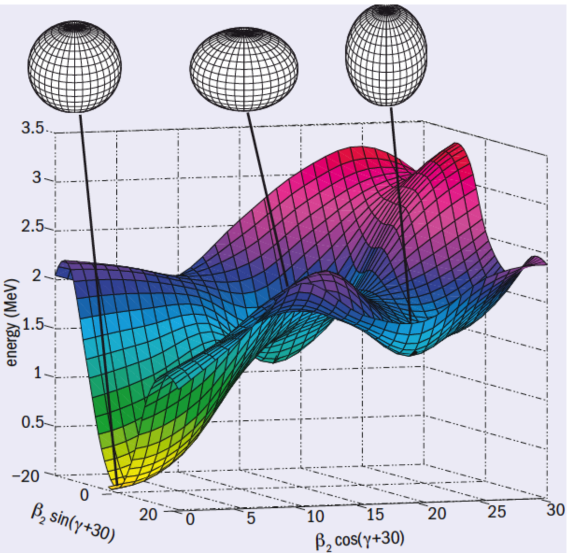

**Figure 2.2:** Potential energy surface plot demonstrating shape coexistence within the $^{186}$Pb nucleus. The $\beta_2$ parameter describes the elongation of the nucleus along the symmetry axis. The $\gamma$ parameter refers to the shape of the nucleus, $\gamma$=0 corresponds to a prolate shaped nucleus and $\gamma$=60$^\circ$ to an oblate shape. Spherical, oblate and prolate minima are shown on the plot by thick vertical black lines. Figure taken from [21].

Another case of shape coexistence occurs in the neutron-deficient region, specifically $^{186}$Pb. The three lowest states of the nucleus were discovered to be spherical, oblate and prolate. Refer to figure 2.2 for a potential energy surface plot of the $^{186}$Pb nucleus, with positions of the spherical, oblate and prolate minima shown.

# Chapter 3

# Experimental setup

This chapter discusses the setup used in this particular experiment, of which the data was collected at the Isotope mass Separator On-Line DEvice (ISOLDE) facility at CERN in June 2016. The ISOLDE facility's purpose is to produce a wide range of radioactive ion beams for various experiments in the fields of nuclear and atomic physics, solid-state physics, materials science and life sciences. During this experiment protons were impinged upon a target, reaction products were selectively ionised using the resonance ionisation laser ion source (RILIS). These ions were accelerated towards one of two mass separators, after separation ions were transported to one of three detection stations. The key method used for this thesis was the KU Leuven Windmill. The Windmill allowed the $\alpha$ decays of the Bi nuclei to be detected and analysed.

## 3.1 ISOLDE/RILIS

### 3.1.1 Beam/Target

A proton beam was fired at a uranium carbide (UCx) target with a thickness of 50 g/cm$^2$, with an intensity of 2.1 $\mu A$ and energy of 1-1.4 GeV [22]. Proton beam pulses are produced by the Proton Synchrotron Booster (PSB), which is a stack of four small synchrotrons, before being aimed at one of the two ISOLDE targets. The beam used consists of 2.4 $\mu s$ proton pulses, with a spacing of 1.2 s. A sequence of pulses is known as a super-cycle, the number of proton pulses can be varied. Figure 3.1 shows an overview of the ISOLDE experimental set-up used [23, 24]. Once the proton beam interacts with one of the targets used, various radioactive nuclei are produced via spallation, fission and fragmentation reactions [22].

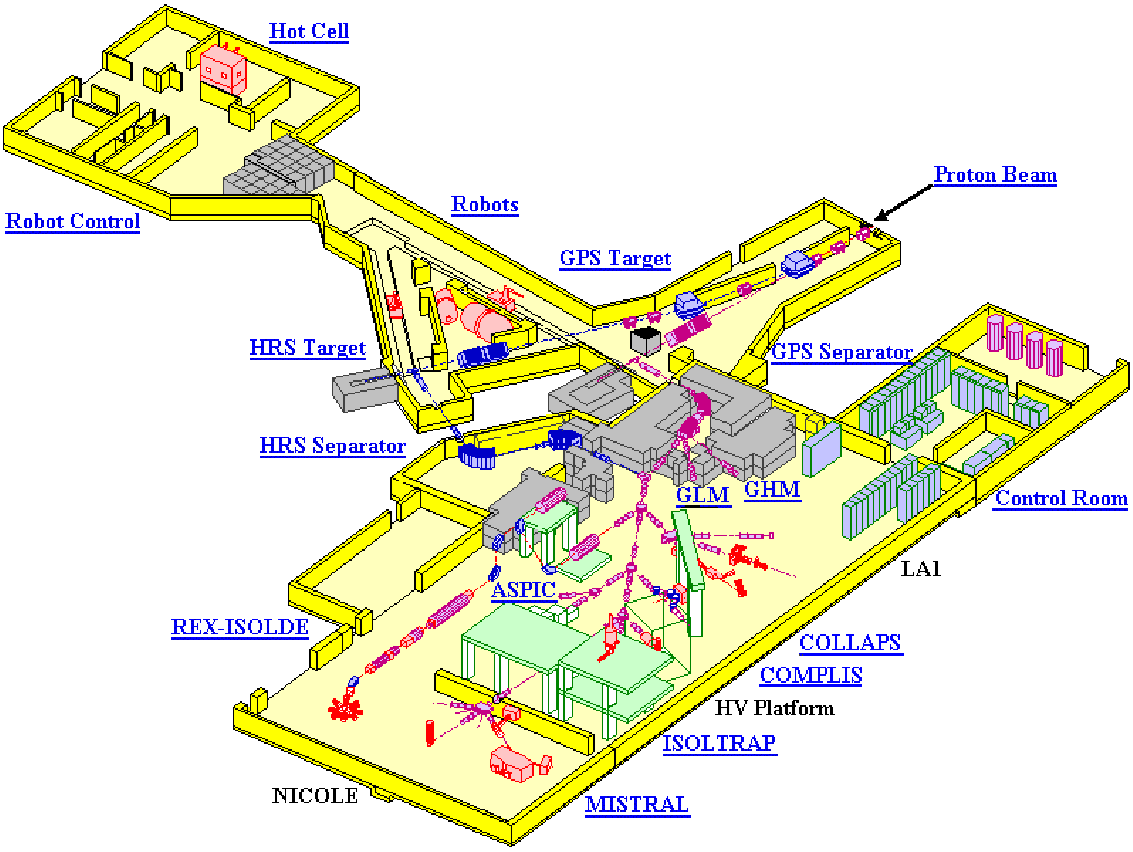

**Figure 3.1:** Layout of the ISOLDE facility [25]. The proton beam enters at the top right to interact with one of the two targets shown; General Purpose Separator (GPS) target or the High Resolution Separator (HRS) target. The KU Leuven windmill is situated to the right of COLLAPS.

### 3.1.2 Ion source

Reaction products diffuse through the target material and effuse into the hot cavity. Refer to figure 3.2 for an overview of the steps involved throughout this experiment. High temperatures of approximately 2300K are used in order to reduce the release time. An issue with utilising such a high temperature, is that isotopes with a low surface ionisation potential can be ionised, resulting in contamination of the beam. Within the cavity, the resolution of the spectra can be affected by Doppler broadening of atomic lines due to thermal motion of the atoms. This is more of a problem for lighter nuclides, however, the heavier isotopes can experience broadening greater than 1 GHz. Selective ionisation using RILIS occurs within the hot cavity [22, 24].

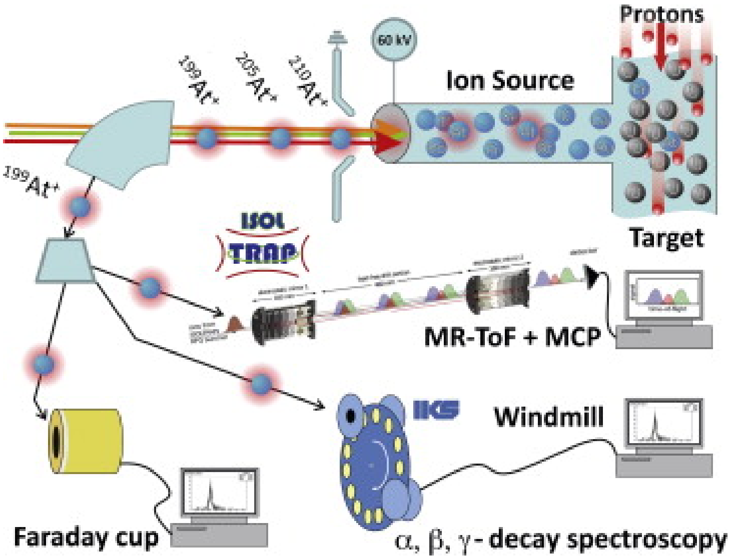

**Figure 3.2:** Overview of the setup used showing three photo-ion detection methods. Figure taken from [24].

RILIS is the main ion source used at the ISOLDE facility. This type of laser ion source utilises two concepts: individual elements have unique atomic energy level distributions; and transitions of electrons between these levels can be incited if a photon with a matching energy is delivered to the atom. A three step ionisation process was exploited throughout this experiment, multiple lasers from RILIS excited the atoms within the hot cavity freeing a valence electron from the atom in question. RILIS can operate in two modes, broad-band (BB); the low resolution mode, and narrow-band (NB); the high resolution laser. In broad-band mode, the laser line width ranges from 10-20 GHz, large enough for a mixture of isotopes and isomers to be ionised and extracted. When using narrow band mode greater selectivity can be achieved. This is due to a laser line width of 1 GHz, being scanned over a range of frequencies in close proximity to one of the transition energies [22, 26]. By doing this individual isomers of the nucleon were selected. The laser which excites the atom from the atomic ground state to the first intermediate state is scanned across a range of frequencies in NB mode in order to scan across the HFS. The other two lasers are not scanned but are in BB mode. Using lasers in BB mode ensures that any atom excited from the ground state can reach continuum. Due to the exclusive distribution of atomic energy levels within an element, an ionisation scheme for each element must be tested and developed [24, 26].

Six tuneable lasers form the RILIS dual Titanium:Sapphire-Dye (Ti:Sa) laser setup, three of which are Ti:Sa the other three are dye lasers. Throughout the experiment the lasers used ran at a frequency of 10 kHz, these were pumped by frequency doubled Nd:YAG (532 nm) laser. The dye lasers could also be UV pumped at 355 nm [22, 26].

The RILIS lasers are installed 20m away from the hot cavity ion source, where selective ionisation takes place. Once the isotopes of interest are ionised to a 1+ state, they are then accelerated by a 30-60 keV potential. Both the target and ion source are seated on an ISOLDE front-end, this is kept at a voltage ranging from 20-60 kV. Approximately 60 mm from the end of the ion source is a grounded extraction electrode [23].

### 3.1.3 HRS/GPS

The two targets used were the General Purpose Separator target and the High Resolution Separator target. A benefit of having two targets available within the ISOLDE experimental hall allows a continuous experiment, whilst one target is being changed the other can be running, reducing downtime [23]. The ions are extracted from RILIS, accelerated by a 60 keV electric field and then separated according to their mass-to-charge ratio using the magnetic dipoles of the GPS or the HRS. The HRS is capable of producing a single mass separated beam with a resolving power of 5000 (M/ΔM). Whereas the GPS provides three beams and has a mass resolving power of 1000. After mass separation one of three methods of analysis were used within the experimental hall [22].

## 3.2 Measurements

### 3.2.1 Windmill

One method of analysis used, was with the KU Leuven Windmill setup. The spectra shown in this thesis was produced from the Windmill data. The laser-ionised and mass-separated beam is delivered to the windmill through a hole in an annular silicon detector (Si1). The beam is implanted into one of ten carbon foils of 20 $\mu$g/cm$^2$ thickness. A second Si detector (Si2) is placed 3 mm behind the foil, see figure 3.3 [27]. The carbon foils (6-10 mm diameter) are mounted on a wheel that is rotated using a stepping motor after each super-cycle. Rotation of the wheel allows implantation in a new foil and longer lived nuclides to be measured, using the additional detectors Si3 and Si4, at the decay site, refer to figure 3.4. The silicon detectors cover a solid angle of 50-66%. Using this geometry provided effective measurements of both single and coincident particle decays from the implanted samples. Surrounding the Windmill are two high purity germanium detectors, Ge1 and Ge2. Ge1 is a planar germanium detector located behind Si2. Ge2 is a single crystal high purity germanium detector located 90° to the beam direction, contributing a 3% efficient at 1 MeV [24]. The Ge detectors used in this experiment differ from the Ge detectors shown in figure 3.3, however, both the Miniball Ge Cluster setup, and the Ge detectors previously mentioned can be utilised with the same outcome.

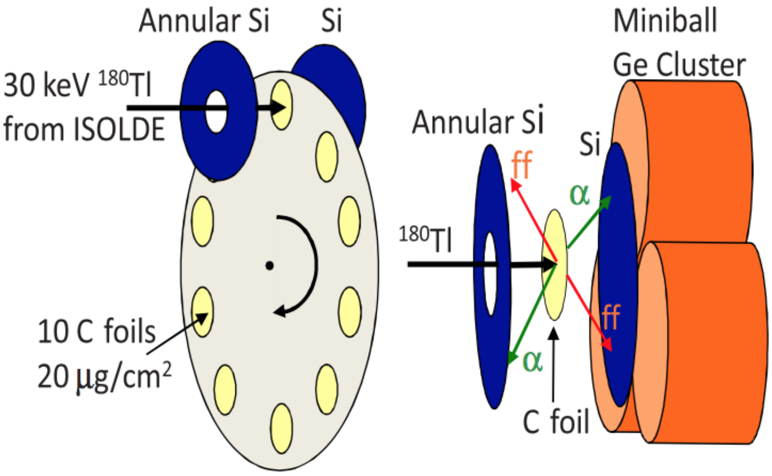

**Figure 3.3:** Overview of the windmill set-up used showing the carbon foils and detector layout. Figure taken from [28].

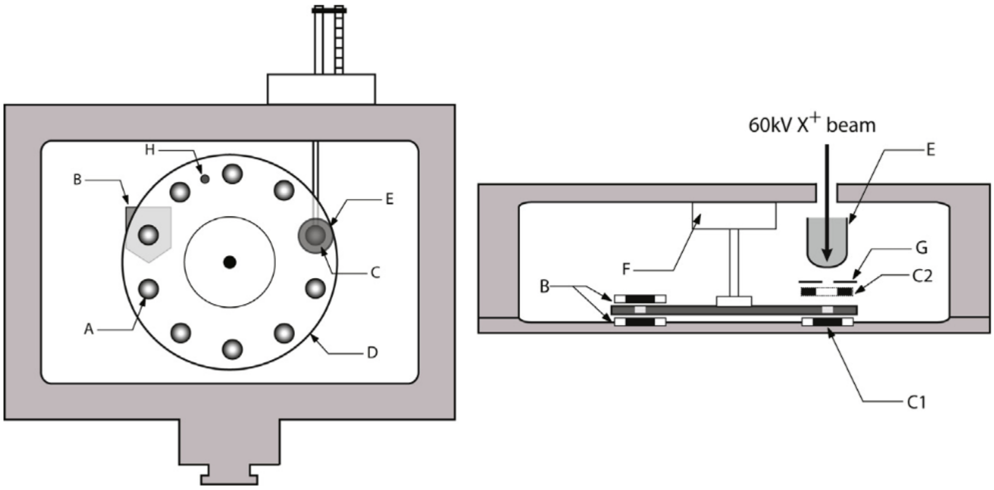

**Figure 3.4:** The KU Leuven Windmill. Carbon catcher foils (A) are mounted on a wheel (D) that is rotated using a stepping motor (F). Movable Faraday cup (E), collimator (G). Two silicon detectors (C1 and C2) measure the alpha spectrum during implantation on the foil, another pair of detectors (B) measure the activity of a previously implanted foil. A $^{241}$Am source (H) is used for calibration purposes. Figure taken from [24].

### 3.2.2 MR-TOF MS

The multi-reflection time-of-flight mass spectrograph (MR-ToF-MS) can be used in cases where the isotope has no alpha decay, a long half-life or there are high levels of contaminants in the beam. MR-ToF consists of two ion-optical mirrors which the ions in question oscillate between and are separated depending on their different mass-over-charge ratios m/q. See figure 3.5 for an overview of the set-up. Flight paths of several hundreds of metres are executed by oscillating between the mirrors, in order to fit an equipment length of approximately one metre. A mass-resolving power m/Δm in the order of $10^5$ was achievable during this experiment. However, the mass resolving power is dependent upon the flight time of the ions [29].

The purpose of MR-ToF is the removal of contaminants in the ion bunch before injection into the dual Penning trap precision mass measurement system. This is achieved by delivering ion bunches to the MR-ToF-MS from the ISOLTRAP linear radio-frequency quadrupole (RFQ) cooler/buncher. The isobar components are separated based on their total flight time for thousands of oscillations within the electrostatic mirror system followed by fast gating using a Bradbury Nielsen gate. The device itself is around 0.8 m long and so the thousands of oscillations between the coaxial electrostatic mirrors results in a long flight path for the ions [30]. Upon release of the ion bunch, if the data acquisition system (DAQ) is also triggered, the isobar components of the ion beam are classed as discrete, isotopically pure ion packets, distinguished by their flight time to the detector. Overall the flight time is tens of seconds, the ion beam components are distributed over multiple seconds [24, 29].

Hence the MR-ToF MS is a fast and selective device for acquiring background free laser scans from low purity ion beams. However MR-ToF can only be used at low ion currents otherwise flight paths will begin to arc.

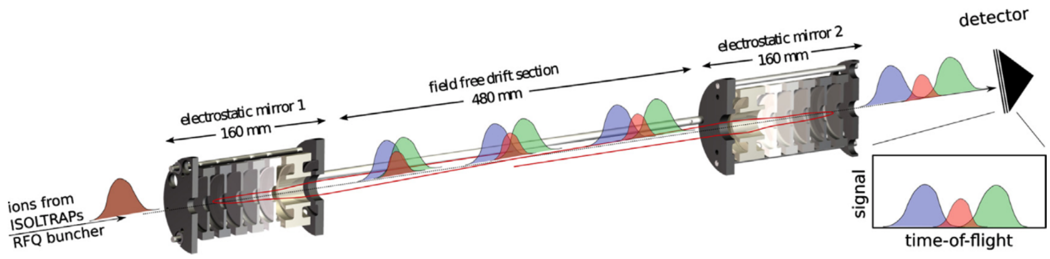

**Figure 3.5:** Overview of the MR-TOF set-up used at ISOLDE. An ion bunch enters from the left, oscillates between the two electrostatic mirrors before an isotopically pure ion bunch is ejected to the right. Figure taken from [24].

### 3.2.3 ISOLDE Decay Station (IDS)

During the IS608 part II experiment in June 2017, in which the author of this thesis took part, the ISOLDE Decay Station (IDS) setup was utilised along with Windmill for the first time. This allowed further possibilities for detailed nuclear spectroscopy studies using $\alpha/\beta/\gamma$ spectroscopy [31]. The IDS is a permanent setup at ISOLDE focused on measuring decay properties of radioactive nuclei of importance with regards to nuclear structure, nuclear engineering and astrophysics. Alpha, beta and gamma radiation were detected using IDS. For $\gamma$-ray detection a MiniBall HPGe cluster and four HPGe clovers are utilised. A variety of setups can be attached to the station for specialised decay measurement, for example fast timing measurement of the lifetimes of excited states, proton and alpha particle emission, and neutron time of flight energy spectroscopy. The station provides tools perfect to study nuclear properties regardless of their location on the nuclear chart [32].

IDS accepts ions from GPS (HRS can also be used) and is located at the end of the beamline. Ions in question are implanted onto tape inside the vacuum chamber once, after passing through a variable aperture collimator. The timing of the movement of the tape can be varied. During the IS608 II, the tape moved with every supercycle in order to be in sync with RILIS. This tape is hundreds of metres in length therefore, unlike Windmill, it is unlikely you would introduce a point on the tape that has previously been implanted on. Within the chamber are four HPGe detectors directed at the centre, with liquid nitrogen cooling canisters. Each detector consists of four HPGe crystals, giving IDS a total of 16 crystals. The IDS setup measures at the implantation position only, there is no secondary position. This can be compared with the windmill setup which, has the decay position to measure the longer lived daughter nuclei [33].

Faraday cups (FC) are used to characterise the beam and focus it onto the implantation tape. A collimator and a movable FC are located at the entrance of the chamber and another FC at the exit. Regarding the silicon detectors, Si telescopes are utilised, which are a stack of two or more detectors to get a wide range of energy measurements with the greatest efficiency. The four Si telescopes have a range of thicknesses between 40 $\mu$m-1.5 mm, to optimise the detection of charged particles colliding with the detectors at a range of energies. Thin Double-sided silicon strip detectors (DSSDs) were chosen in order to not be affected by $\beta$ radiation but thick enough to stop low energy charged particles. Particles with higher energies reach the second layer of the telescope hence, make it possible to detect low energy particle emission thus identity the particle. The thick DSSDs completely stop particles of higher energy but have a high response to $\beta$ particles that hinder the lower energy identification. The fifth, thick horizontal strip in the DSSD, focuses on $\beta$ detection, which is positioned below the tape station [34].

# Chapter 4

# Decay Spectroscopy and HFS Results

The following chapter will present the data collected during the IS608 part I experiment, conducted in June 2016 at ISOLDE. From this data our understanding of the Bi nucleus can be improved. During this run the carbon foils were continuously implanted. This prohibited the calculation of half lives, however HFS data was used to establish the presence of two isomers, from which the isotope shift could be calculated.

## 4.1 $^{191}$Bi Analysis

Two scans were completed during the $^{191}$Bi run; file 0146 and 0147_0148. As seen in figure 4.1 there are three possible $\alpha$ decays of two states, the ground state and an isomer, in $^{191}$Bi.

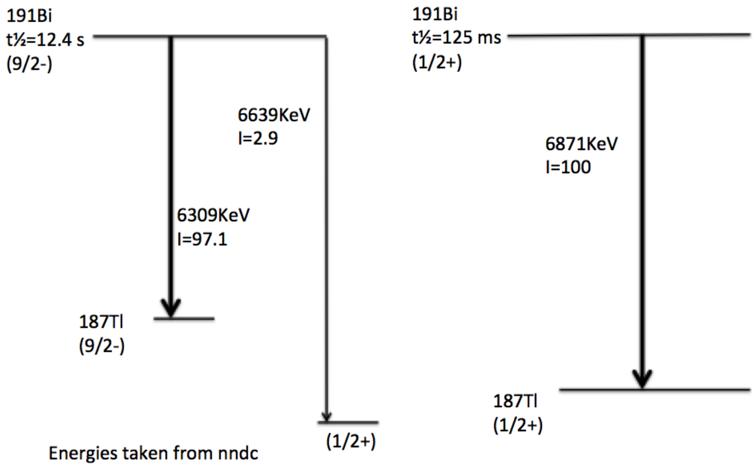

**Figure 4.1:** $^{191}$Bi decay scheme showing all possible alpha decays from both the ground and isomeric state. Half lives ($t_{1/2}$) and relative intensity (I) of transitions also shown.

Figure 4.2 shows the decays detected at the implantation site; in both Si detectors, Si1 and Si2. During both runs three peaks were clearly seen, the highest intensity being the 6309 keV decay from the ground state(9/2-) of $^{191}$Bi to the isomer state of $^{187}$Tl (9/2-). A second peak seen at 6639 keV is of lower intensity, this is due to an alpha decay from the ground state of $^{191}$Bi to the ground state (1/2+) of $^{187}$Tl. The final peak occurs at 6871 keV, a decay from the isomer state of $^{191}$Bi to the ground state of $^{187}$Tl.

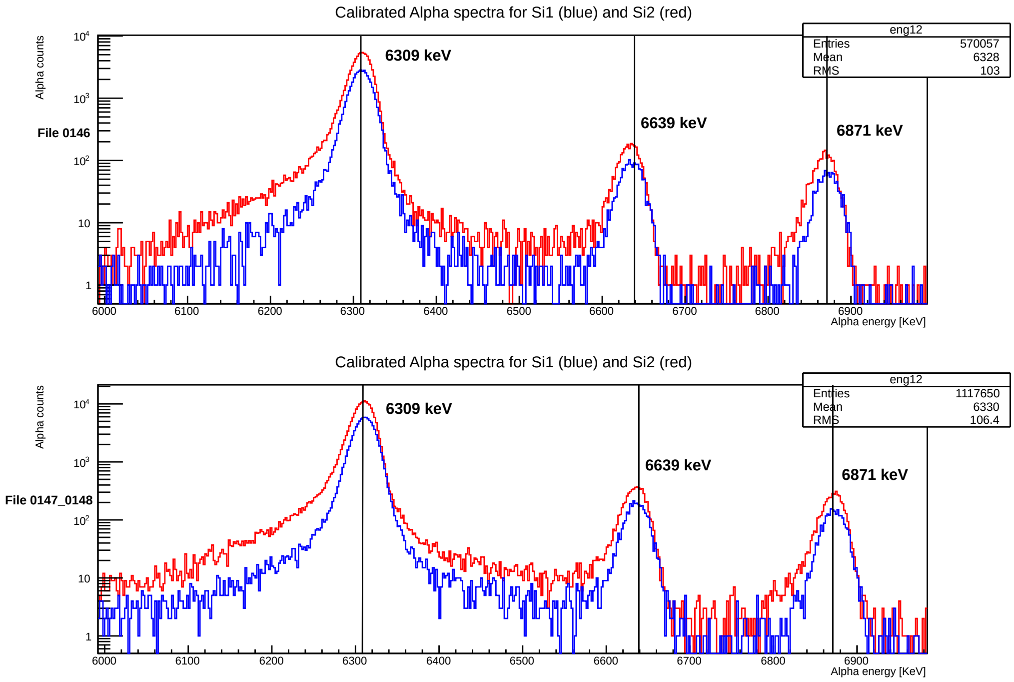

**Figure 4.2:** Alpha spectra of $^{191}$Bi at implantation site. The three peaks shown are direct alpha decays from $^{191}$Bi to $^{187}$Tl. Peaks shown at 6309 keV and 6639 keV are ground state decays whereas the peak at 6871 keV is from an isomeric state. The top panel represents the alpha spectra seen during run 146 and the lower panel is for the combined run of 147 and 148.

Once the alpha spectra was obtained energy gates were placed around individual peaks in order to gain the HFS plot seen in figure 4.3. The upper panel displays the energy gate in pink, from 6280 keV to 6330 keV. The RILIS laser scanned across the range of the desired transition, decays at each laser frequency step were detected and recorded. The lower panel displays the HFS seen in both Si1 and Si2, the counts in Si1 are always lower. This scan increased in wavenumber from 10862.259520 $\text{cm}^{-1}$ to 10862.800030 $\text{cm}^{-1}$ with a run time of 3432 s, at 1 supercycle (SC) per step, with a total of 109 steps. The right hand peak in the lower panel is not a perfect gaussian shape this is due to the peak consisting of multiple individual peaks, refer back to section 1.3 for a more in depth explantion. We can deduce that the slight dip in the right hand peak is the result of three peaks differing in intensities leading to the asymmetry seen. This asymmetric shape will persist throughout all the files for this decay.

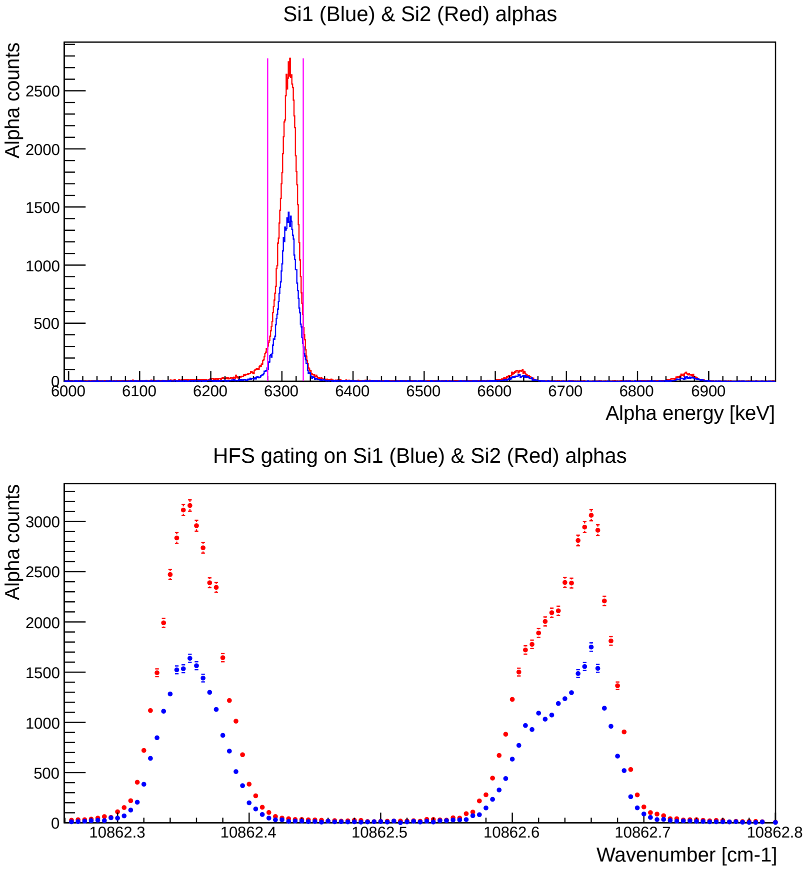

**Figure 4.3:** HFS for file 0146 of $^{191}$Bi. Energy gate placed around the 6309 keV peak (9/2- state) to produce the HFS seen at the implantation site.

Figure 4.4 shows two plots, the upper being the laser power during this particular scan, the lower plot is the proton current at each step. Laser power and proton current must remain relatively constant whilst scanning, any drops in laser power/proton current will affect the data collected.

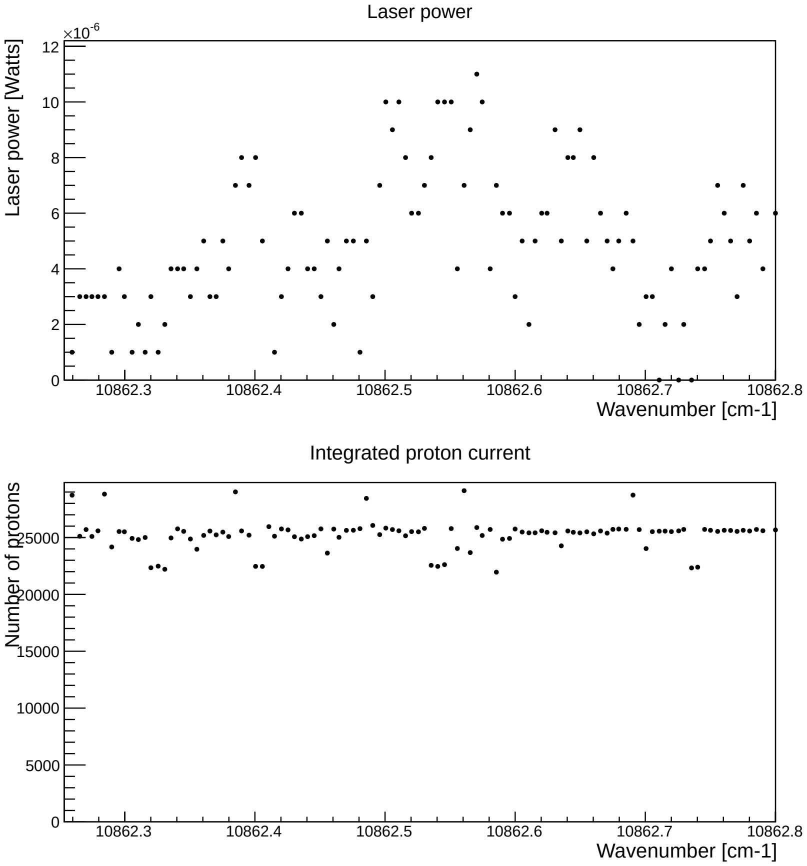

**Figure 4.4:** Laser power and proton current for file 0146 of $^{191}$Bi.

The 6639 keV peak was then gated from 6610 to 6660 keV, shown in pink in figure 4.5. This peak has much lower counts than the 6309 keV decay by a factor of 30. The shape of the HFS plot produced should be similar to the decay at 6309 keV but lower in intensity/counts. For each run all peaks were gated to produce the HFS seen in the figures, along with the laser power and proton current plots.

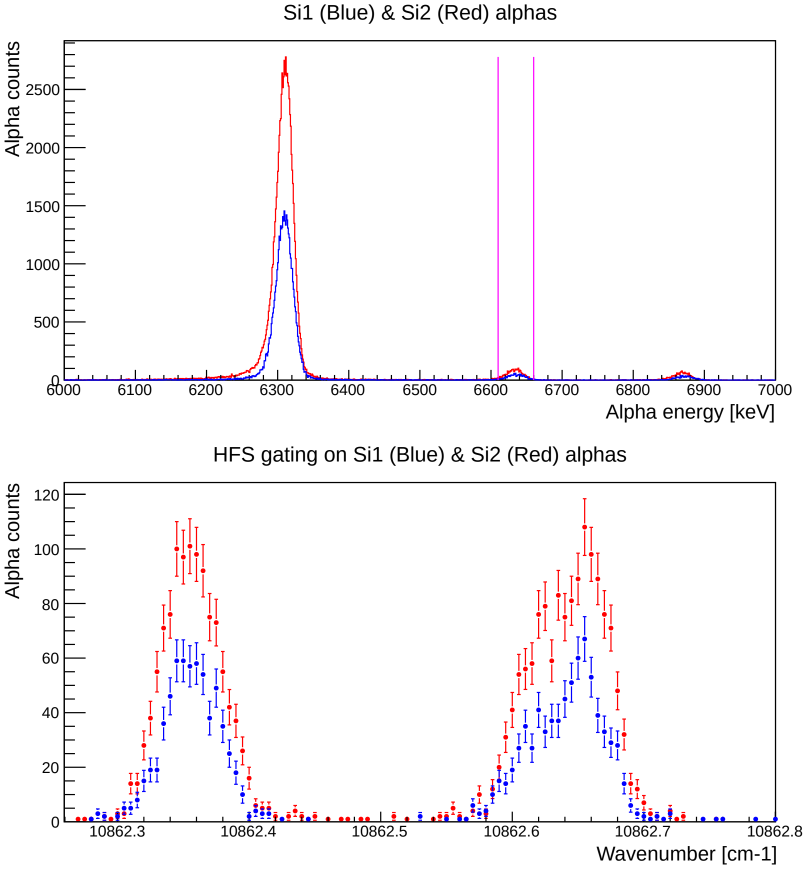

**Figure 4.5:** HFS for file 0146 of $^{191}$Bi. Energy gate placed around the 6639 keV peak (9/2- state) to produce the HFS seen at the implantation site.

The final peak to be gated was the isomeric state of Bi (1/2+), from 6845 to 6890 keV, as seen in figure 4.6. The peak seen on the left in the lower panel is not made up of multiple peaks unlike previous HFS plots, however, the right hand peak consists of two peaks.

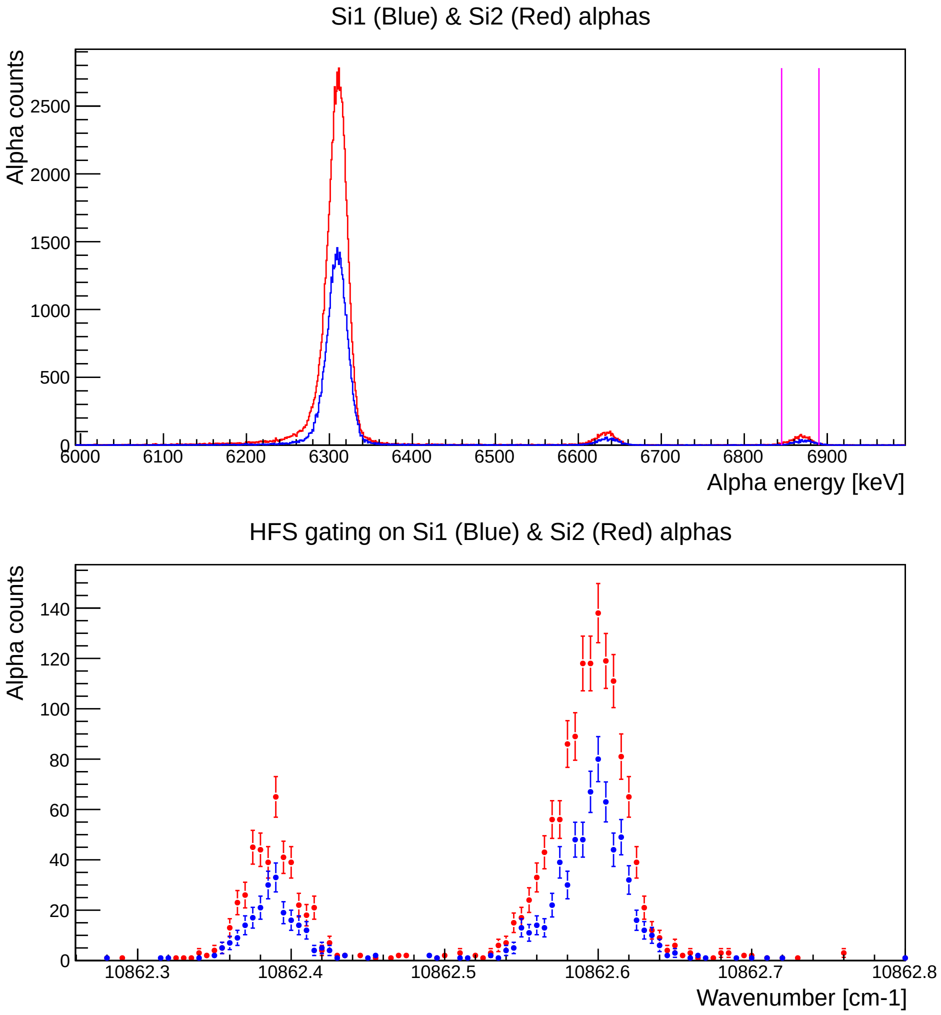

**Figure 4.6:** HFS for file 0146 of $^{191}$Bi. Energy gate placed around the 6871 keV peak (1/2+ state) to produce the HFS seen at the implantation site.

For file 0147_0148 this scan decreased in wavenumber from 10862.78038 cm$^{-1}$ to 10862.27945 cm$^{-1}$ with a run time of 3629 s, at 1 supercycle (SC) per step, with a total of 91 steps. Just as before each peak was gated and the HFS plot produced.

Once all peaks had been gated from each run an overlap of the HFS spectra was produced. Initially spectra produced from each run would be overlaid with the same isomer in order to see the final shape of the HFS. Figure 4.7 shows the overlap of the HFS of the isomeric state (1/2+).

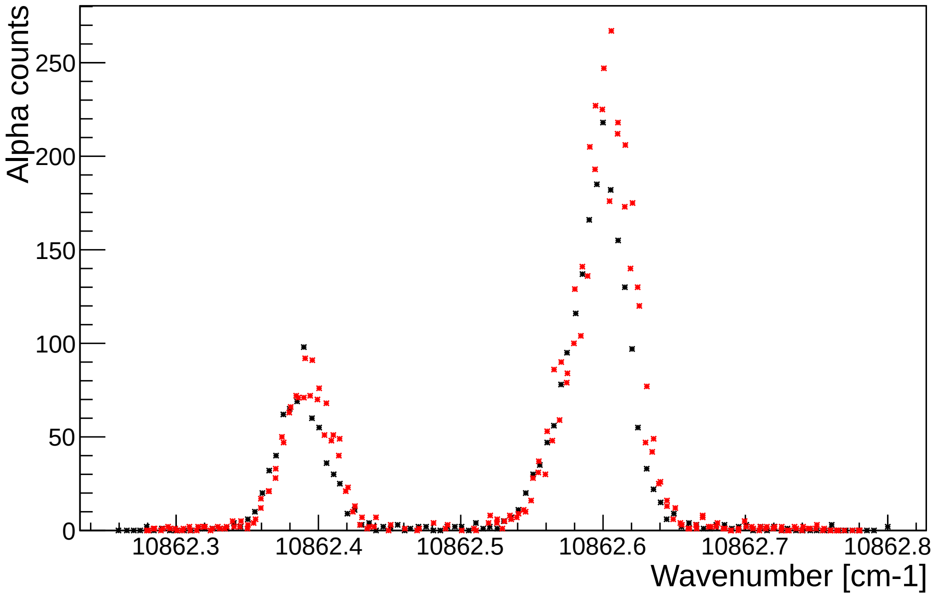

**Figure 4.7:** Overlap of HFS from files 0146 (black points) and 0147_0148 (red points) of the Isomeric state(1/2+) of $^{191}$Bi. There is a very slight shift between scans, this could be a result of the accuracy of the calibrations.

By creating an overlap of the HFS of the ground, and an overlap of the HFS of the isomer, the shift in centre of gravity becomes more apparent. The centre of gravity for the isomeric state seen in figure 4.7 is at 10862.54 cm$^{-1}$, whereas the centre of gravity of the ground state is at 10862.52 cm$^{-1}$. With regards to the 9/2- isomer of Bi there are two possible decays from this state, the 6309 keV decay reaches 5000 counts whereas the 6639 keV decay only has a maximum counts of 175. For this case separate overlaps were created as seen in figures 4.8 and 4.9

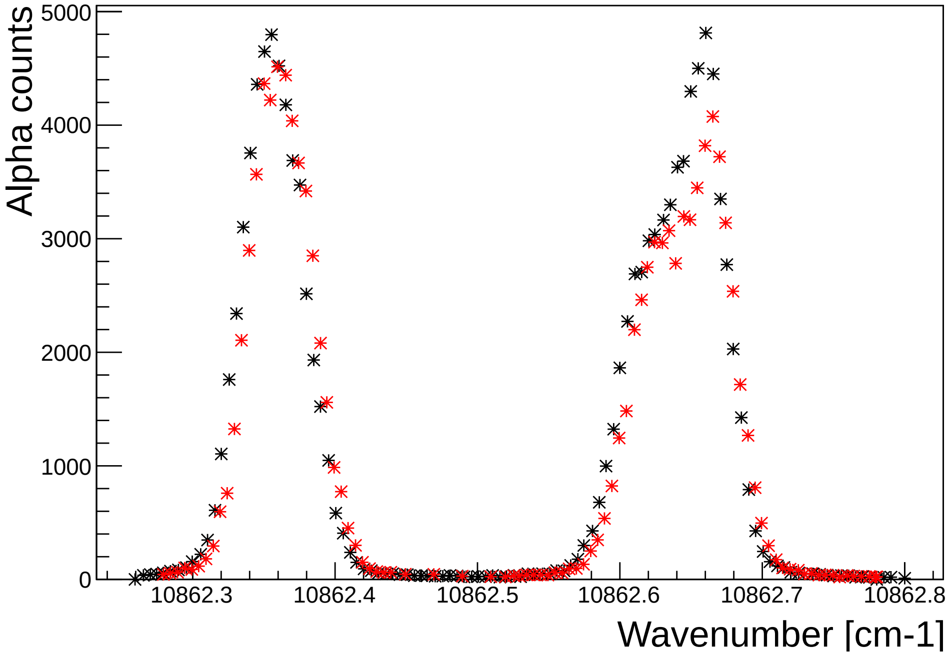

**Figure 4.8:** Overlap of HFS from files 0146 (black points) and 0147_0148 (red points) of the 6309 keV ground state(9/2-) of $^{191}$Bi.

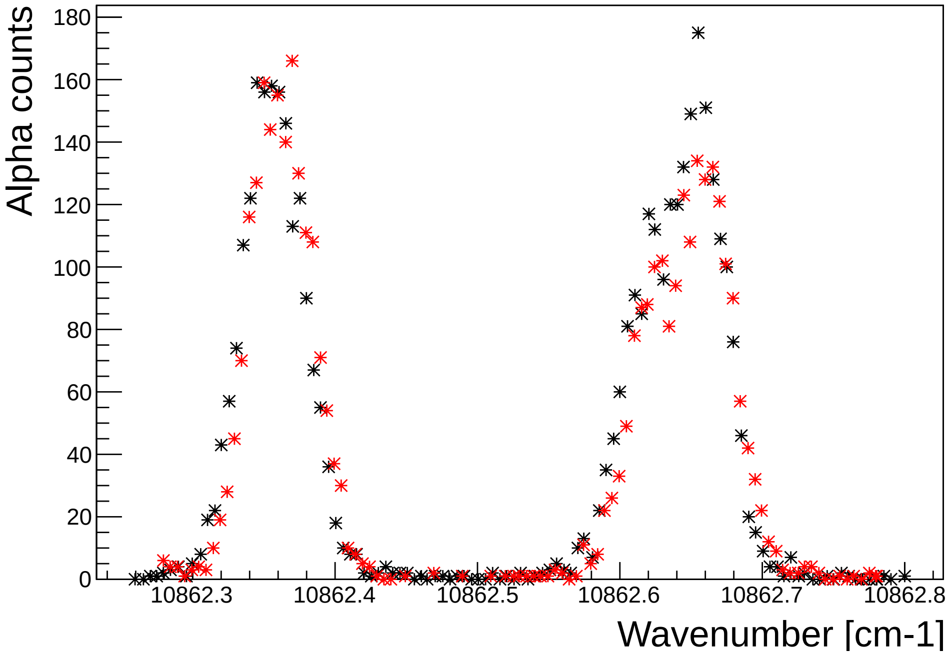

**Figure 4.9:** Overlap of HFS from files 0146 (black points) and 0147_0148 (red points) of the 6639 keV ground state of $^{191}$Bi.

## 4.2 $^{189}$Bi Analysis

There are four files that make up the $^{189}$Bi run, files 0152_0153, 0154, 0155 and 0156. Figure 4.10 shows there are seven possible $\alpha$ decays of two states in $^{189}$Bi.

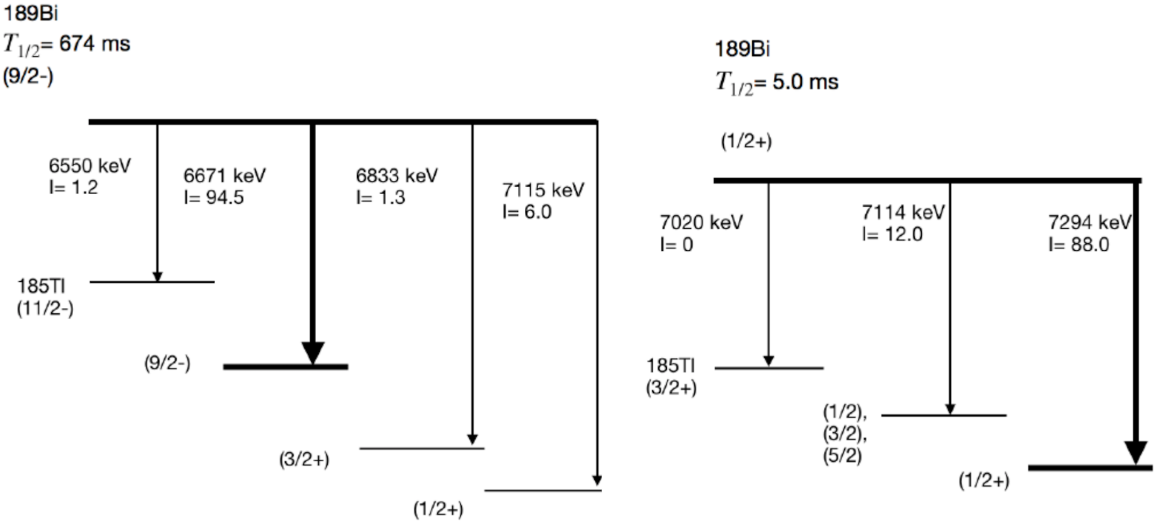

**Figure 4.10:** Decay scheme of $^{189}$Bi showing all possible alpha decays from both the ground state and the isomeric state. Relative intensity (I) and half lives ($t_{1/2}$) given.

Refer to figure 4.11 and 4.12 for the decays detected at implantation site, from $^{189}$Bi to $^{185}$Tl. During these particular runs only two alpha decays of $^{189}$Bi were detected. The most prominent peak occurred at 6671 keV, as a result of an alpha decay from the ground state (9/2-) of $^{189}$Bi to an isomeric state (9/2-) of $^{185}$Tl. The second peak seen in the alpha spectra is a decay from the ground state (9/2-) of $^{189}$Bi to an isomeric state (1/2+) of $^{185}$Tl at 7115 keV.

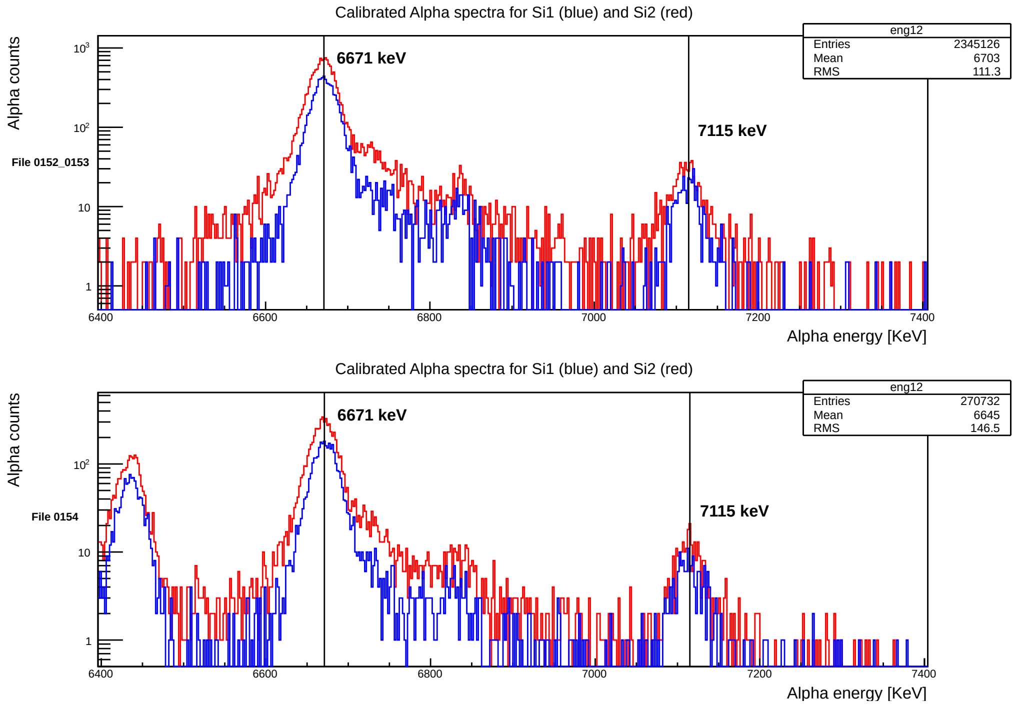

**Figure 4.11:** Alpha spectra of files 0152_0153 (top panel) and 0154 (lower panel) of $^{189}$Bi at implantation site. Contaminant seen in file 0154 at 6434 keV.

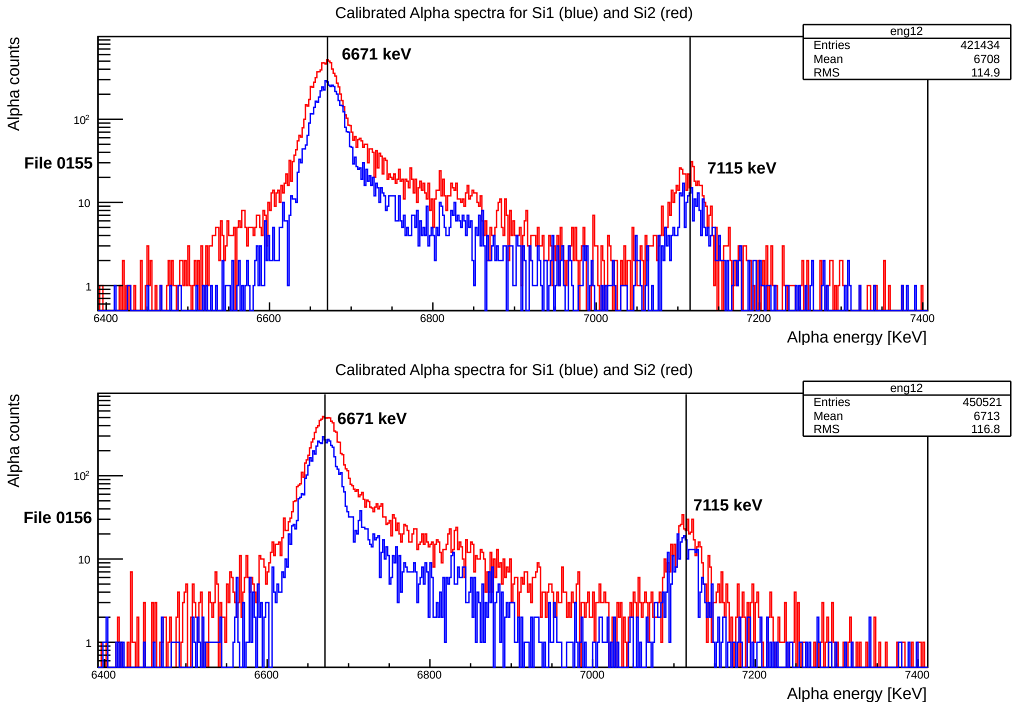

**Figure 4.12:** Alpha spectra of files 0155 (top panel) and 0156 (lower panel) of $^{189}$Bi at implantation site.

Initially the 6671 keV peak (9/2-) was gated from 6630 keV to 6700 keV, in file 0152_0153, shown by the pink lines in the top panel of figure 4.13. Gating this particular produced the HFS spectrum seen in the lower panel of figure 4.13. A drop in alpha counts can be seen at 10862.63 cm$^{-1}$ this is due to a reduced number of protons being supplied at this specific point, which corresponds to the drop seen in the integrated proton current plot in figure 4.14. This scan increased in wavenumber from 10862.230392 cm$^{-1}$ to 10862.760470 cm$^{-1}$ with a run time of 3260 s, at 1 supercycle (SC) per step. In total there were 107 steps for this file.

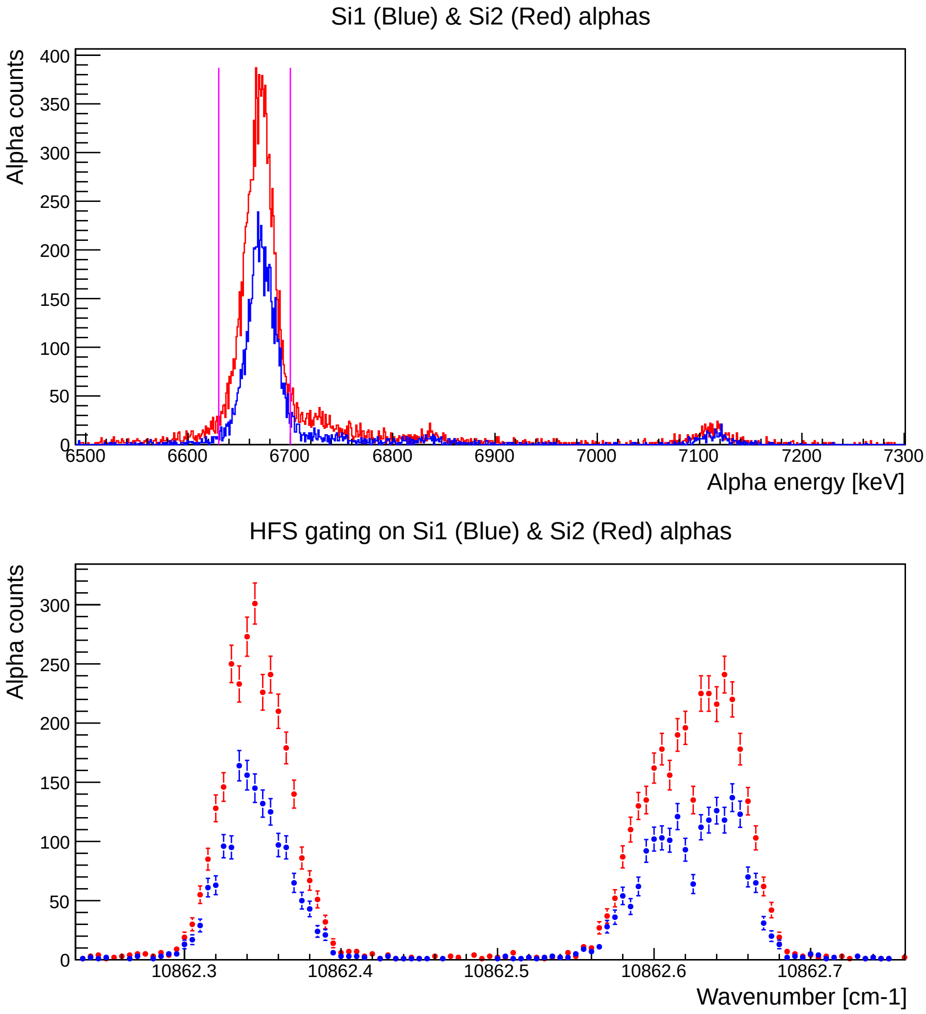

**Figure 4.13:** HFS for file 0152_0153 of $^{189}$Bi. Energy gate from 6630-6700 keV(pink lines) placed around the 6671 keV peak (9/2- state) to produce the HFS seen at the implantation site (lower panel).

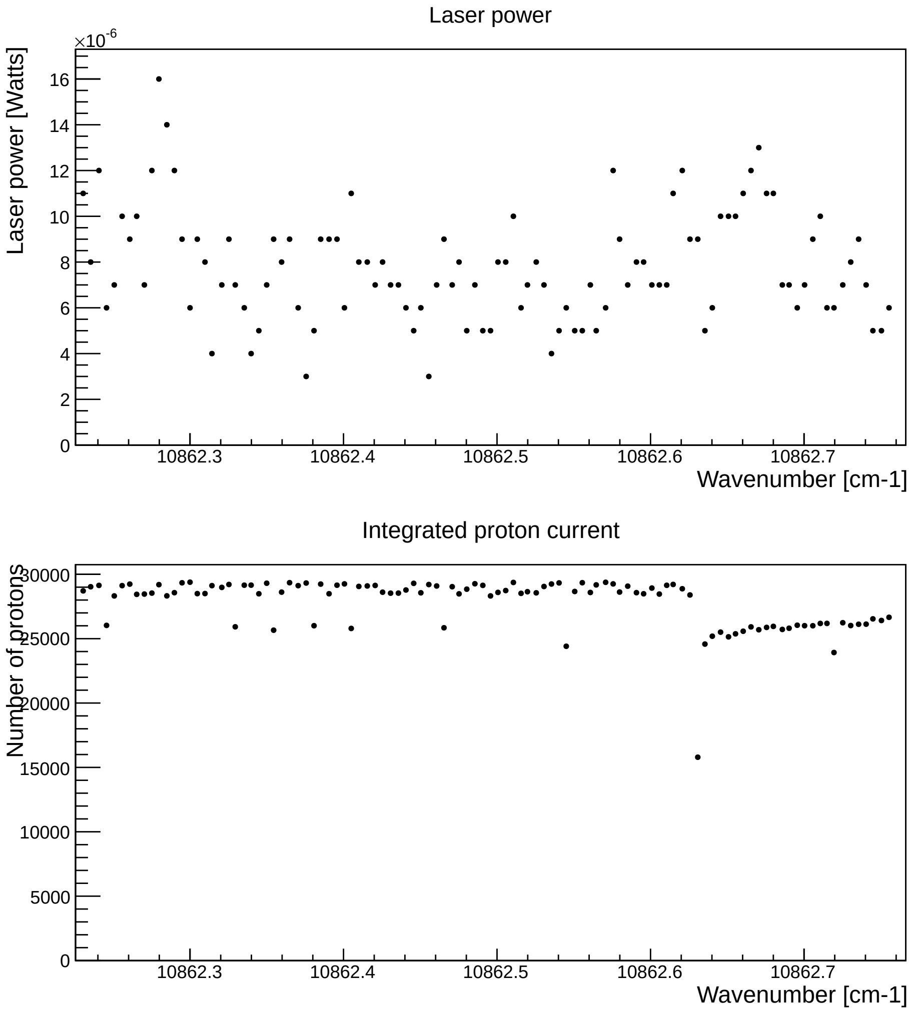

**Figure 4.14:** Laser power and proton current plots for all decays seen in file 0152_0153 of $^{189}$Bi.

The next gate to placed was from 7080 keV to 7140 keV. This peak was due to the decay from the ground state in $^{189}$Bi to an isomeric state of $^{185}$Tl at 7115 keV. Gating this peak resulted in the HFS spectrum provided in figure 4.15. There is a drop in the number of protons supplied, in the lower plot of figure 4.15, at 10862.62 cm$^{-1}$, this was also the case with the previous gate placed in this file.

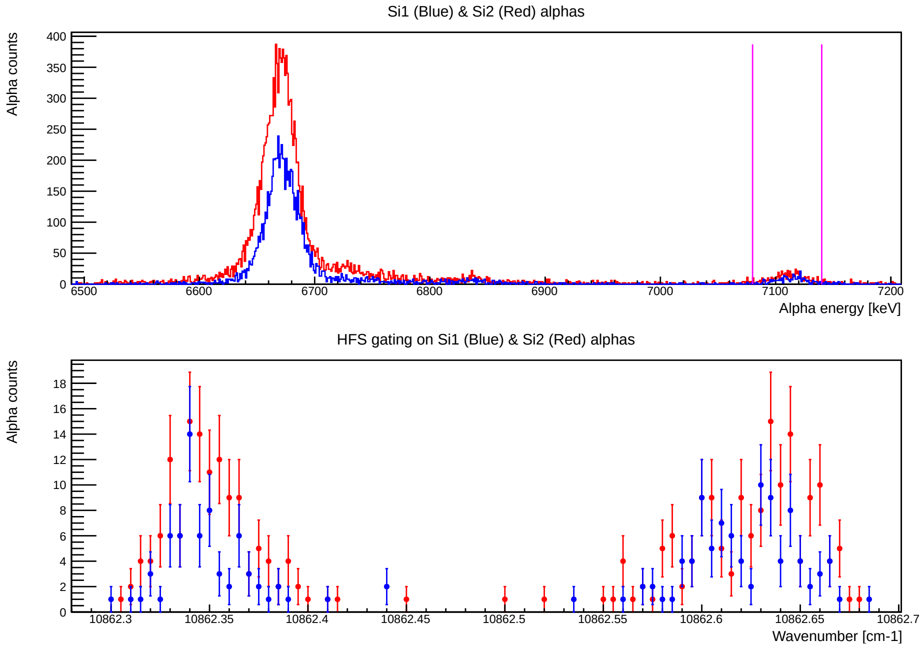

**Figure 4.15:** HFS for file 0152_0153 of $^{189}$Bi. Energy gate from 7080-7140 keV placed around the 7115 keV peak (9/2- state) to produce the HFS seen at the implantation site (lower panel).

During file 0154 there was a shift in calibration of the spectrum leading to the fall in counts of the second peak at 10862.63 cm$^{-1}$ seen in the lower panel of figure 4.16. This issue affects both gates used. This scan decreased in wavenumber from 10862.729619 cm$^{-1}$ to 10862.269648 cm$^{-1}$ and lasted 2740 s, at 1 SC/step, with a total of 86 steps.

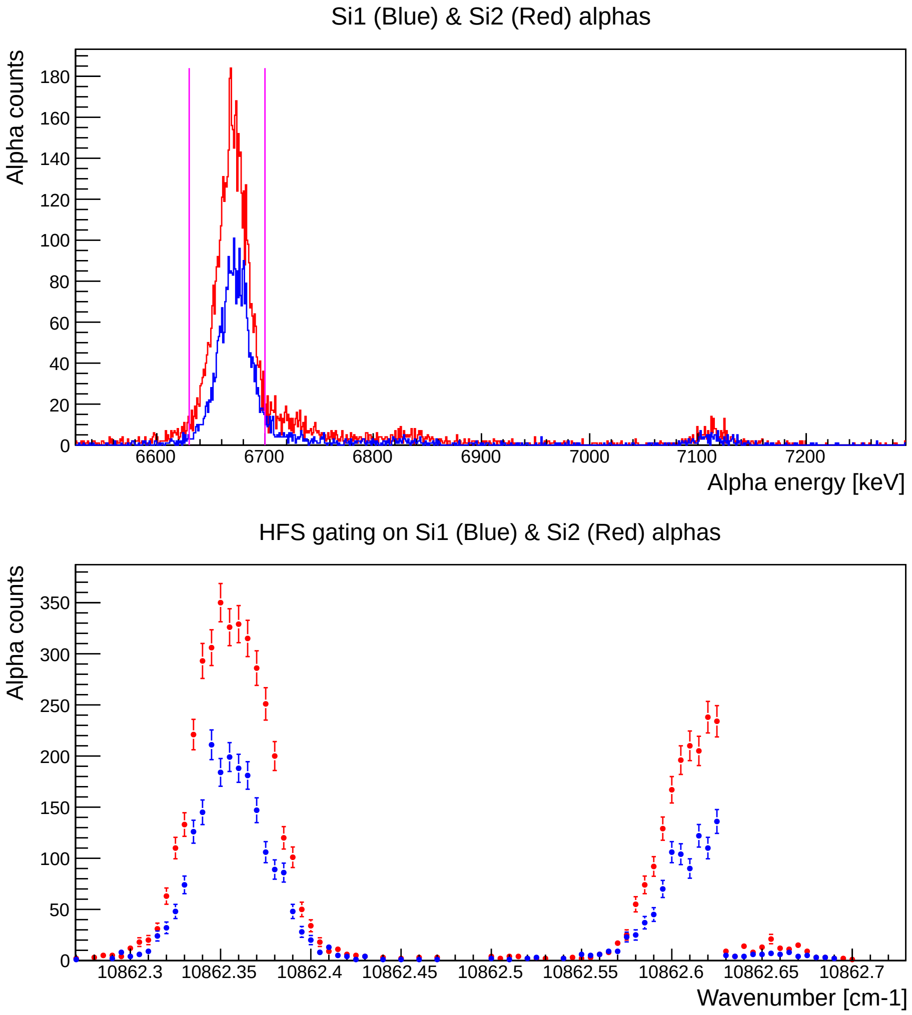
Si1 (Blue) & Si2 (Red) alphas

HFS gating on Si1 (Blue) & Si2 (Red) alphas

**Figure 4.16:** HFS for file 0154 of $^{189}$Bi. Energy gate placed around the 6671 keV peak (9/2- state) to produce the HFS seen at the implantation site (lower panel).

The HFS for file 0155 can be seen in figure 4.17. This scan increased in wavenumber from 10862.250012 cm$^{-1}$ to 10862.730441 cm$^{-1}$ with a runtime of 2845 s, at 1 SC/step, and a total of 90 steps.

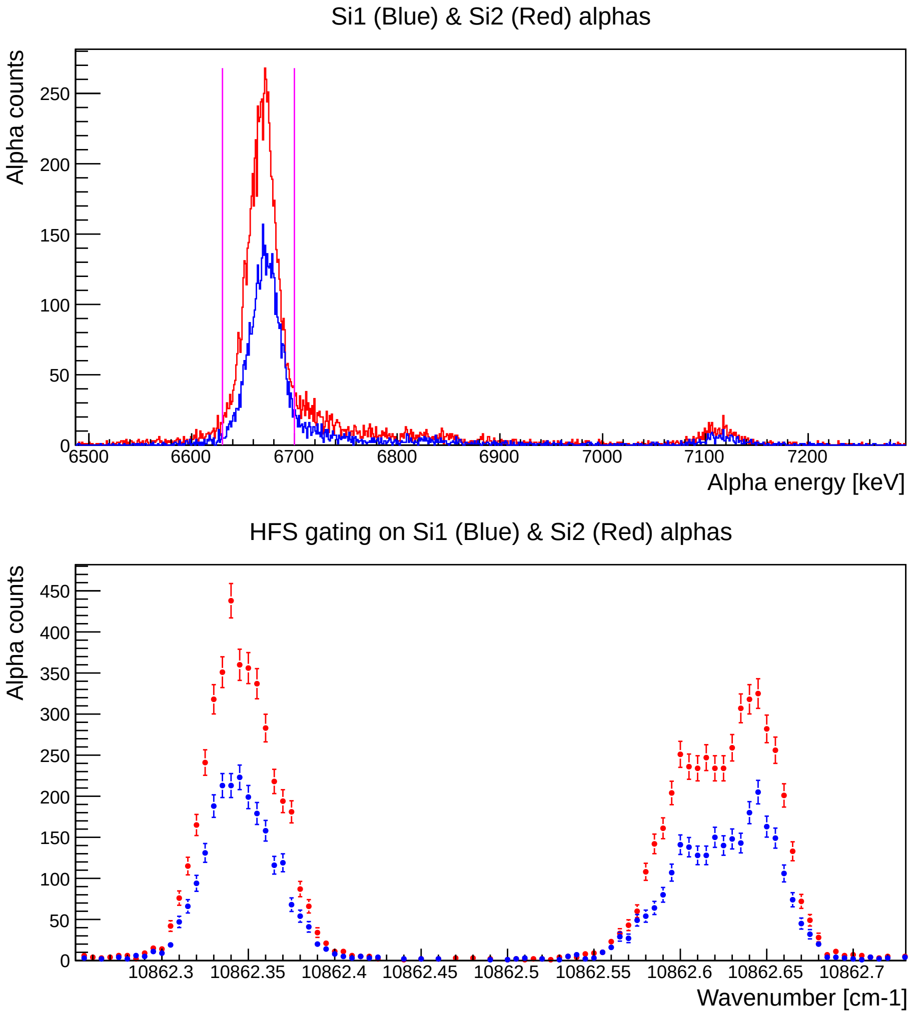

**Figure 4.17:** HFS for file 0155 of $^{189}$Bi. Energy gate placed around the 6671 keV peak (9/2- state) to produce the HFS seen at the implantation site (lower panel).

The HFS for file 0156 is shown in figure 4.18. This scan decreased in wavenumber from 10862.729798 cm$^{-1}$ to 10862.259727 cm$^{-1}$ with a runtime of 2776 s, at 1 SC/step, and a total of 88 steps.

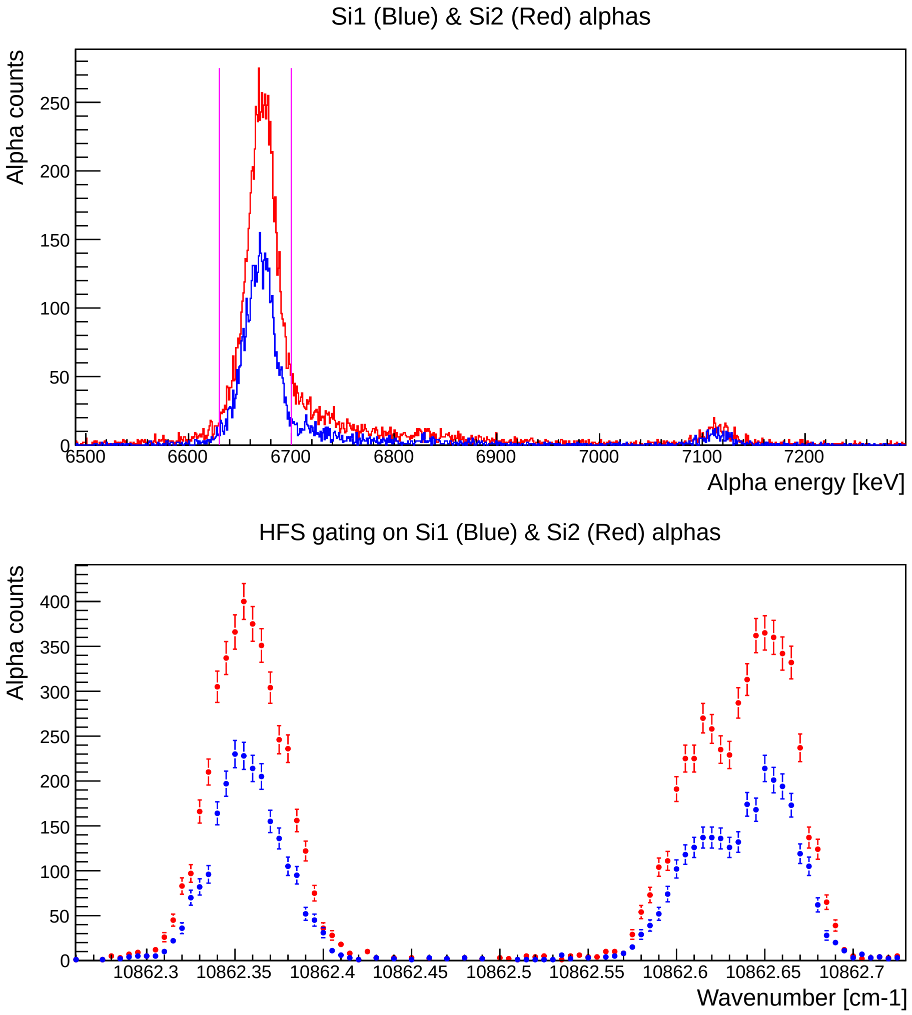

**Figure 4.18:** HFS for file 0156 of $^{189}$Bi. Energy gate placed around the 6671 keV peak (9/2- state) to produce the HFS seen at the implantation site (lower panel).

Refer to figures 4.19 and 4.20 for the overlaps of the HFS of the ground state decays, 6671 keV and 7115 keV respectively.

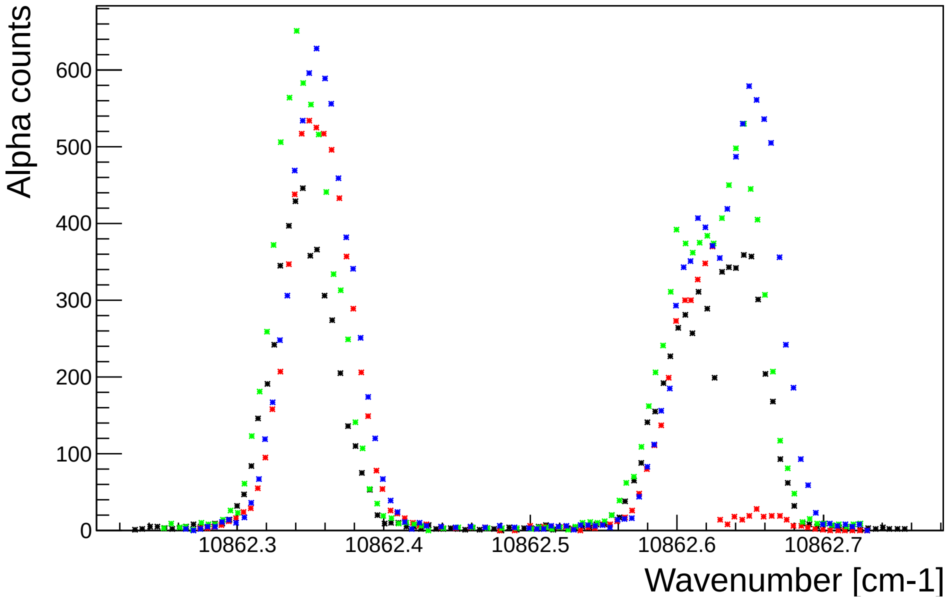

**Figure 4.19:** Overlap of the (9/2-) ground state decays at 6671 keV HFS from all files during the $^{189}$Bi run. File 0152_0153 (black), file 0154 (red), file 0155 (green) and file 0156 (blue).

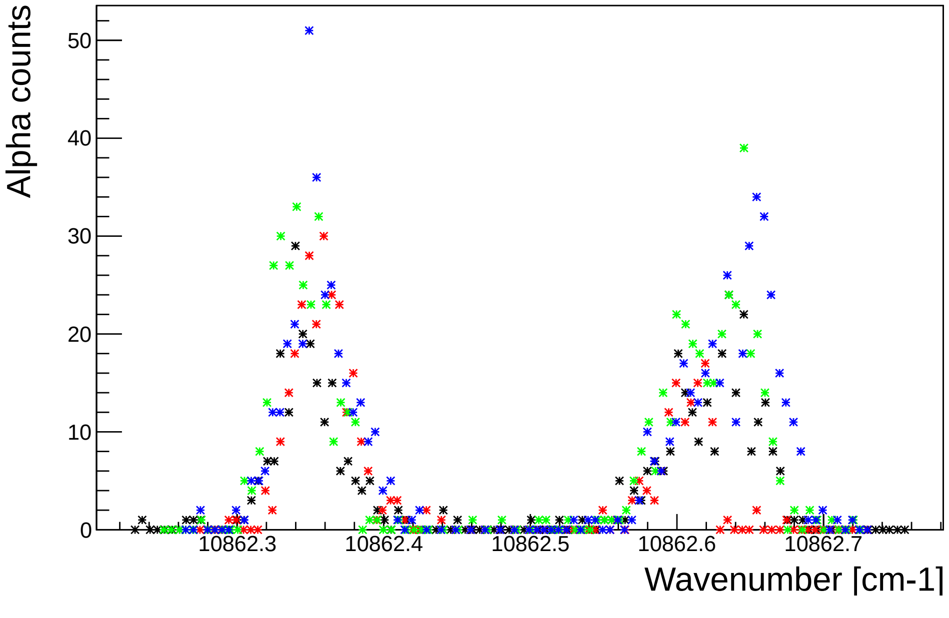

**Figure 4.20:** Overlap of the (9/2-) ground state decays at 7115 keV HFS from all files during the $^{189}$Bi run. File 0152_0153 (black), file 0154 (red), file 0155 (green) and file 0156 (blue).

## 4.3 $^{188}$Bi Analysis

During the $^{188}$Bi run, five scans took place; files 0158, 0159_0160_0161, 0162_0163_0164, 0219_0220 and 0221_0222. Figure 4.21 shows there are seven possible $\alpha$ decays of two states in $^{188}$Bi.

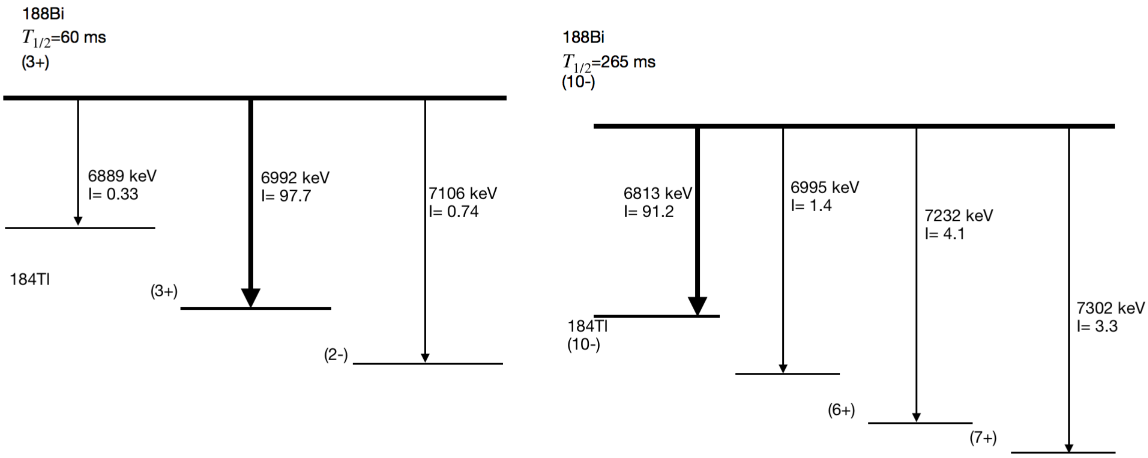

**Figure 4.21:** Decay scheme of $^{188}$Bi showing all possible alpha decays from both the ground and an isomeric state. Relative intensity (I) and half lives ($t_{1/2}$) given.

Figures 4.22, 4.23 and 4.24 display the decays detected at implantation site for each scan. The most noticeable peak being the decay from the ground state (10-) of $^{188}$Bi to an isomeric state (10-) of $^{184}$Tl which occurred at 6813 keV. The second peak present in each scan during this run, was the decay from an isomeric state (3+) of $^{188}$Bi to an isomeric state (3+) of $^{184}$Tl at 6992 keV.

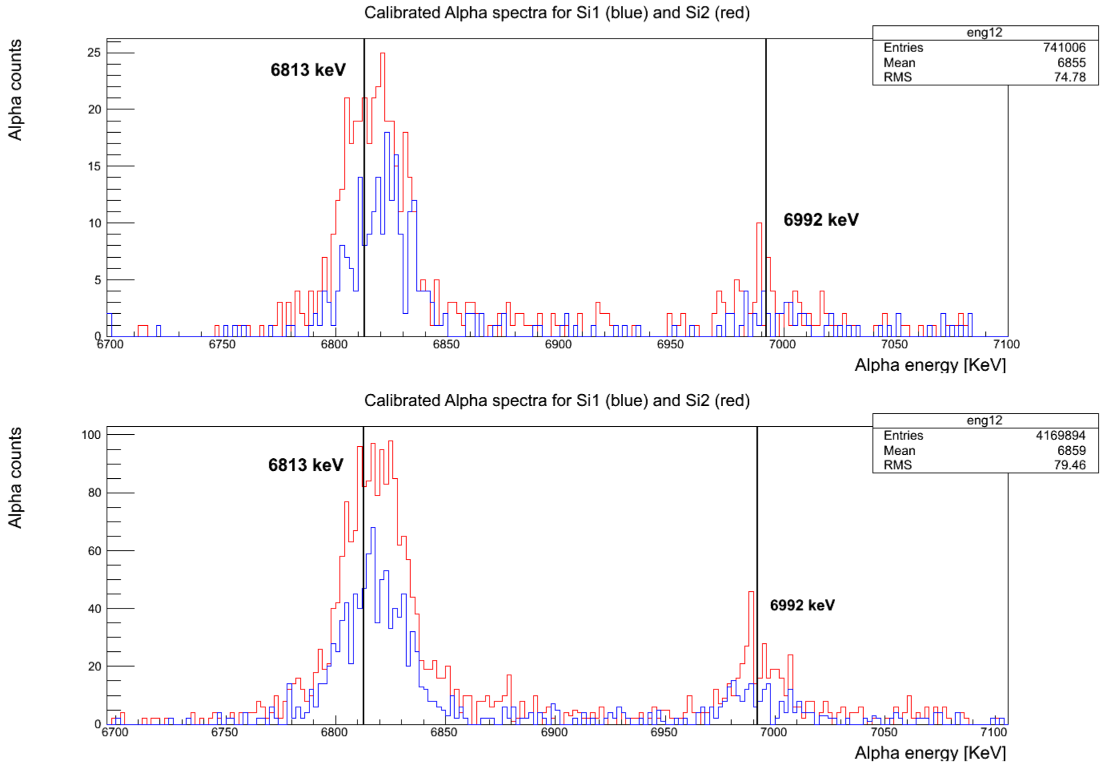

**Figure 4.22:** Alpha spectra of files 0158 and 0159_0160_0161 of $^{188}$Bi.

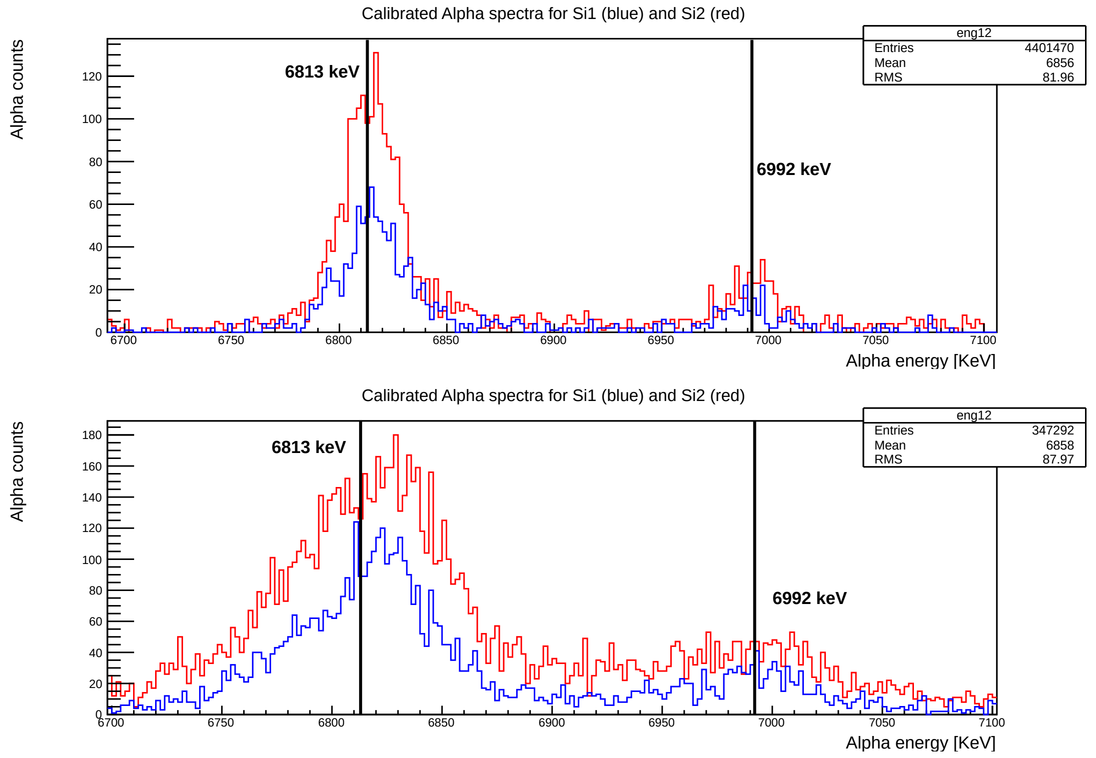

**Figure 4.23:** Alpha spectra of files 0162_0163_0164 and 0219_0220 of $^{188}$Bi.

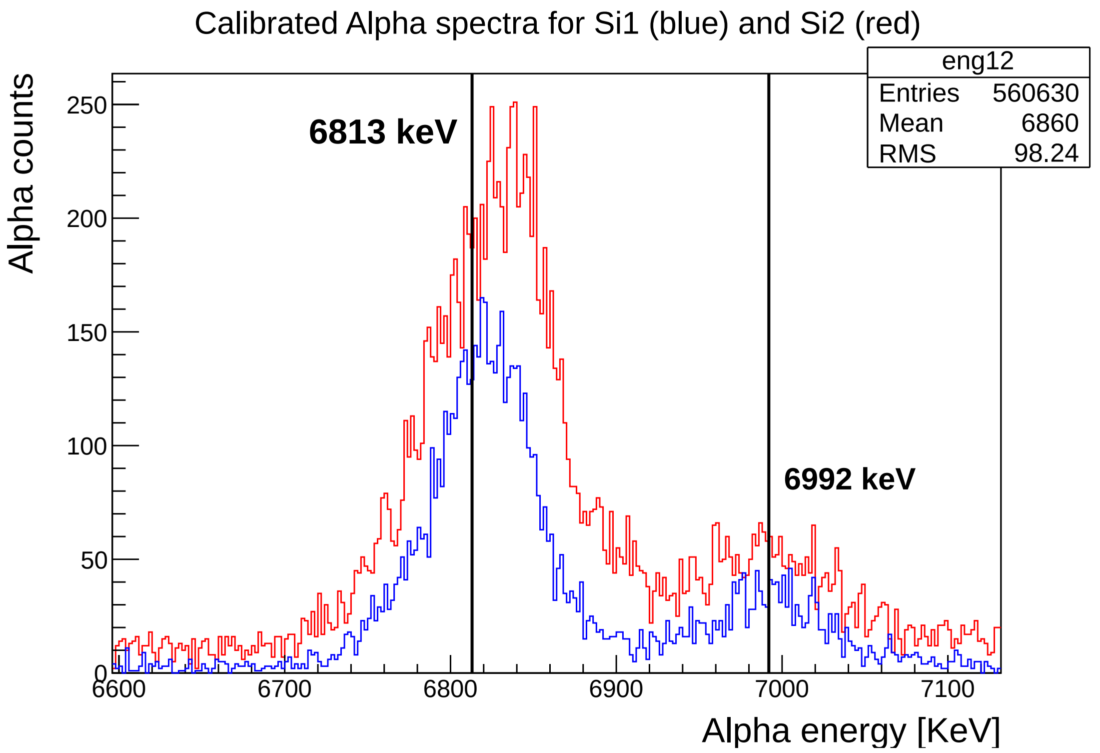

**Figure 4.24:** Alpha spectra of file 0221_0222 of $^{188}$Bi.

During the $^{188}$Bi run there was contamination from $^{188}$Pb at 6000 keV however, gating on this peak resulted in no HFS plot. The peak seen at 6813 keV, the (10-) ground state decay, was gated from 6760 keV to 6850 keV, for file 0158 in order to produce the HFS plot shown in the lower panel of figure 4.25. Scan 0158 increased in wavenumber from 10862.200784 cm$^{-1}$ to 10862.790050 cm$^{-1}$ with a run time of 3717 s, at 1 SC/step. In total there were 119 steps for this file. Refer to figure 4.26 for laser power and proton current plots for file 0158.

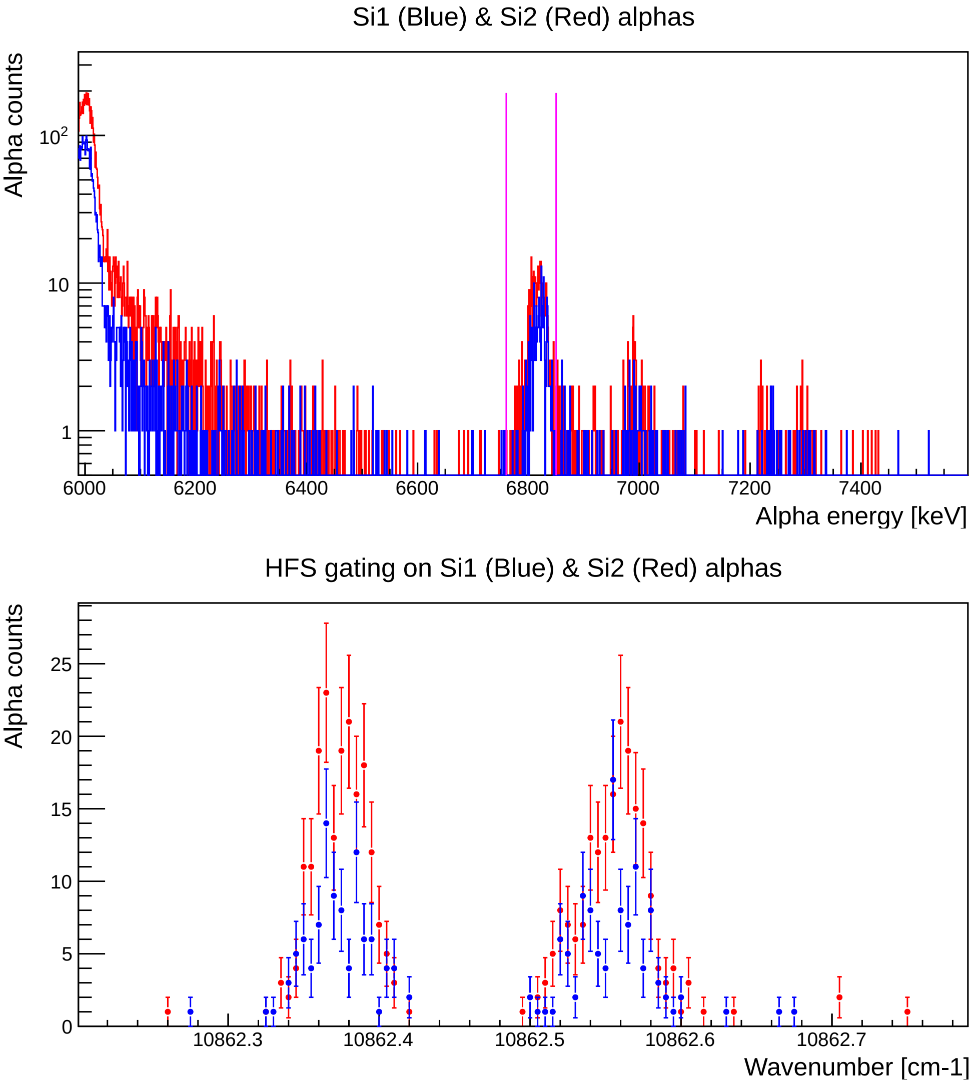
Si1 (Blue) & Si2 (Red) alphas

HFS gating on Si1 (Blue) & Si2 (Red) alphas

**Figure 4.25:** HFS plot for file 0158 of $^{188}$Bi. Energy gate from 6760-6850 keV, shown by the pink lines in the top panel, placed around the 6813 keV peak (10- state) to produce the HFS seen at the implantation site.

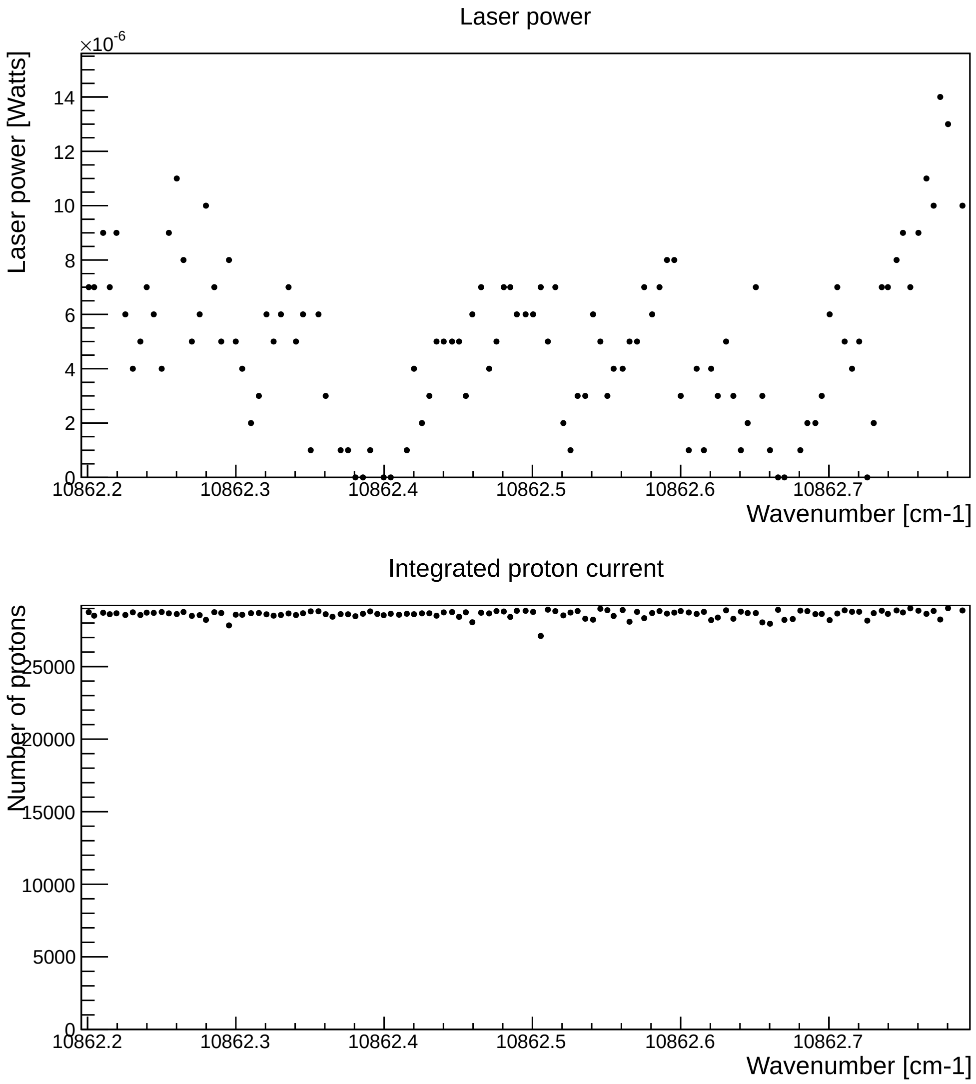

**Figure 4.26:** Laser power and proton current plots for all decays seen in file 0158 of $^{188}$Bi.

Another gate from 6960 keV to 7020 keV, was placed around the 6992 keV peak (3+ isomeric state decay) leading to the HFS plot shown in figure 4.27. At 6995 keV, as shown in figure 4.21, there is another decay from an isomeric state of $^{188}$Bi to an isomeric state (3+) of $^{184}$Tl. This added data points to the (3+) HFS plot from the (10-) decay as the alpha gate contained both peaks.

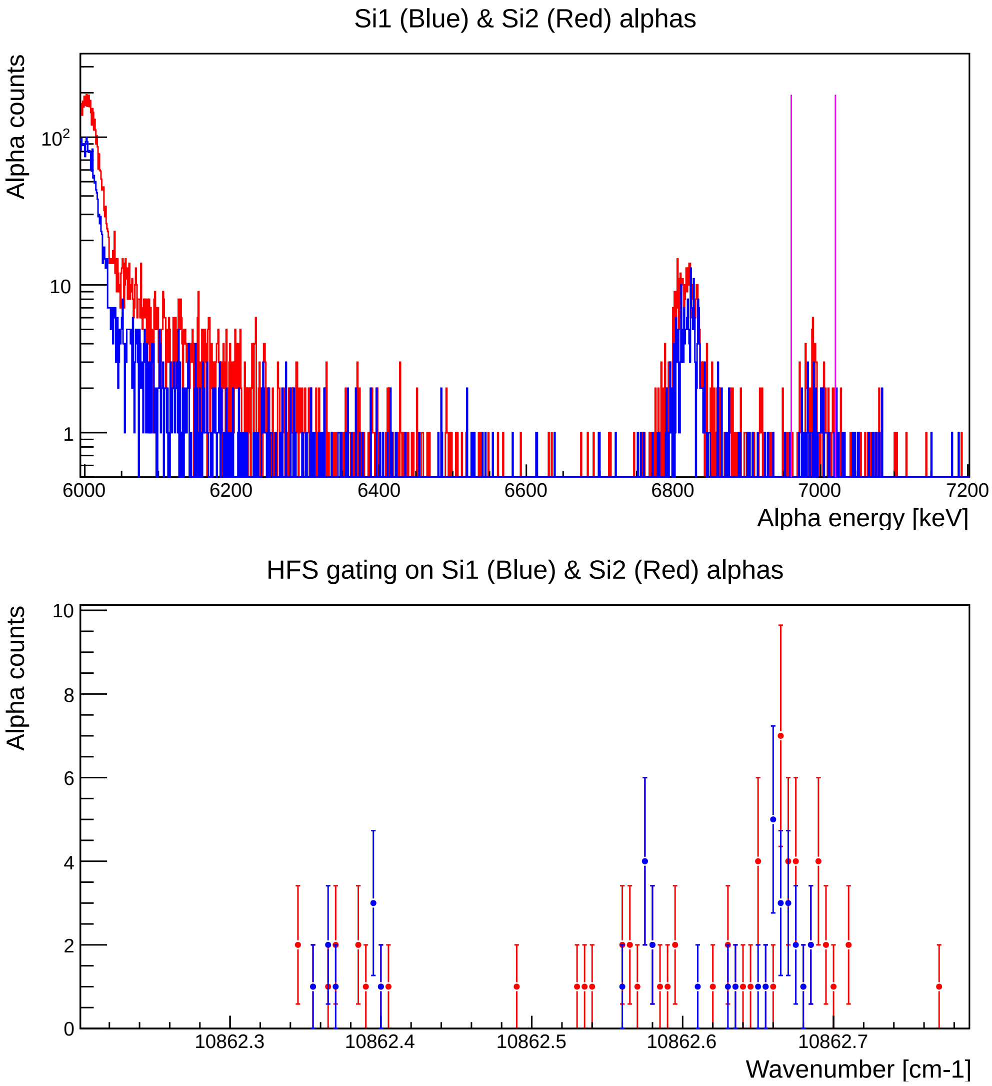

**Figure 4.27:** HFS plot for file 0158 of $^{188}$Bi. Energy gate placed around the 6992 keV peak (3+ isomer) to produce the HFS seen at the implantation site.

The HFS for file 0159_0160_0161 can be seen in figure 4.28. This scan decreased in wavenumber from 10862.789511 cm$^{-1}$ to 10862.099964 cm$^{-1}$ with a run time of 9215.4 s, at 2 SC/step. In total there were 123 steps for this scan.

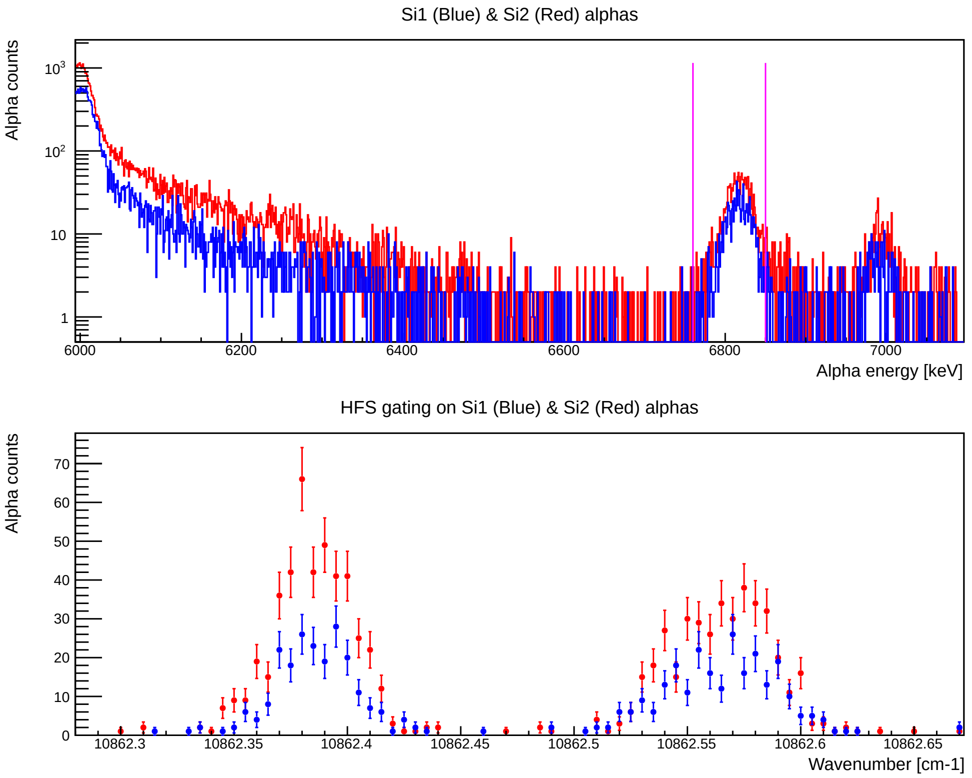

**Figure 4.28:** HFS plot for file 0159_0160_0161 of $^{188}$Bi. Energy gate placed around the 6813 keV peak (10- state) to produce the HFS seen at the implantation site.

The HFS for file 0162_0163_0164 can be seen in figure 4.29. This scan increased in wavenumber from 10862.229345 cm$^{-1}$ to 10862.752367 cm$^{-1}$ with a run time of 9098.5 s, at 4 SC/step. In total there were 59 steps for this scan.

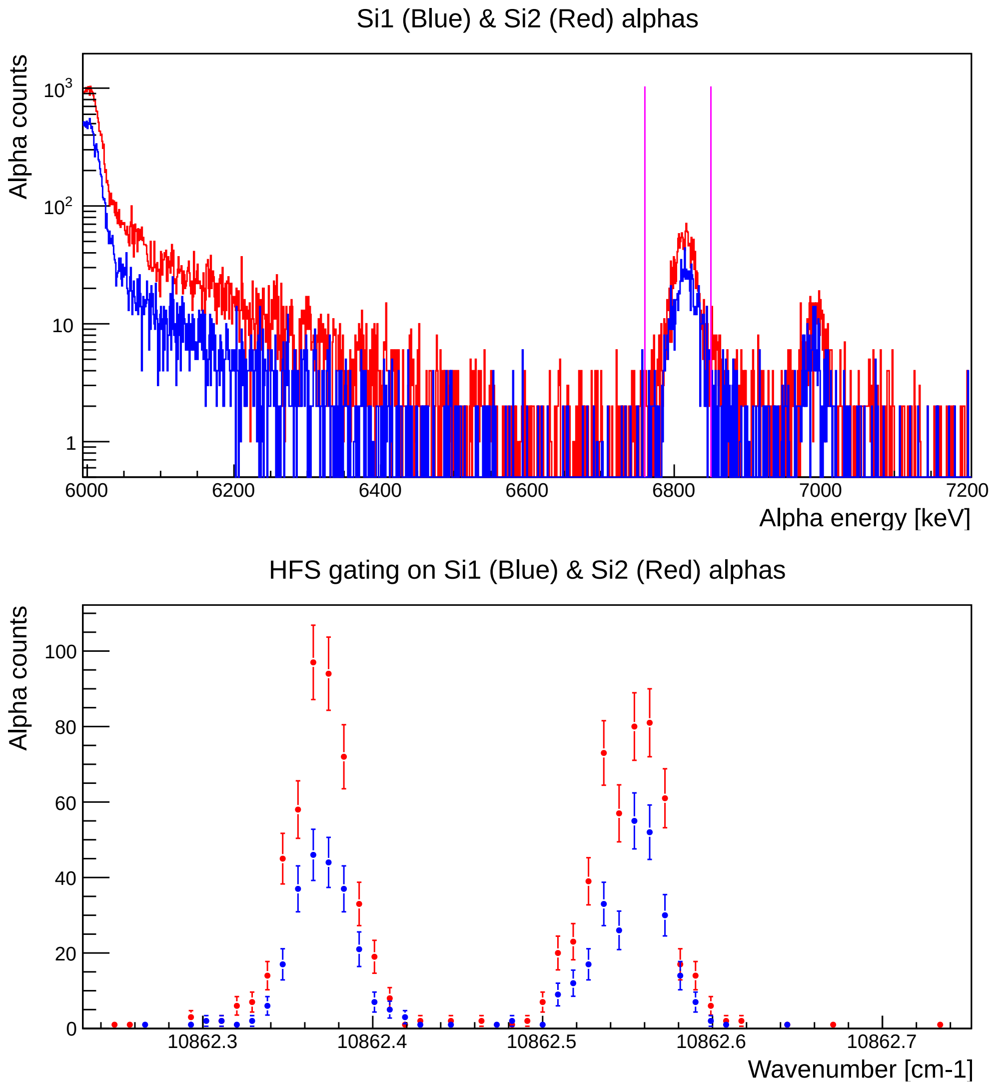

**Figure 4.29:** HFS plot for file 0162_0163_0164 of $^{188}$Bi. Energy gate placed around the peak seen at 6813 keV (10- isomer) in order to produce the HFS seen at implantation site.

The HFS for file 0219_0220 can be seen in figure 4.30. This scan increased in wavenumber from 10862.310551 cm$^{-1}$ to 10862.748670 cm$^{-1}$ with a run time of 14569.8 s, at 3 SC/step. In total there were 74 steps for this scan. For both file 0219_0220 and file 0221_0222 the gate placed on the (10-) ground state decay was increased from 6760-6850 keV to 6760-6890 keV in order to cover the full peak. In this scan a drop in alpha counts is present at 10862.58 cm$^{-1}$ as a result of the decrease in the number of protons.

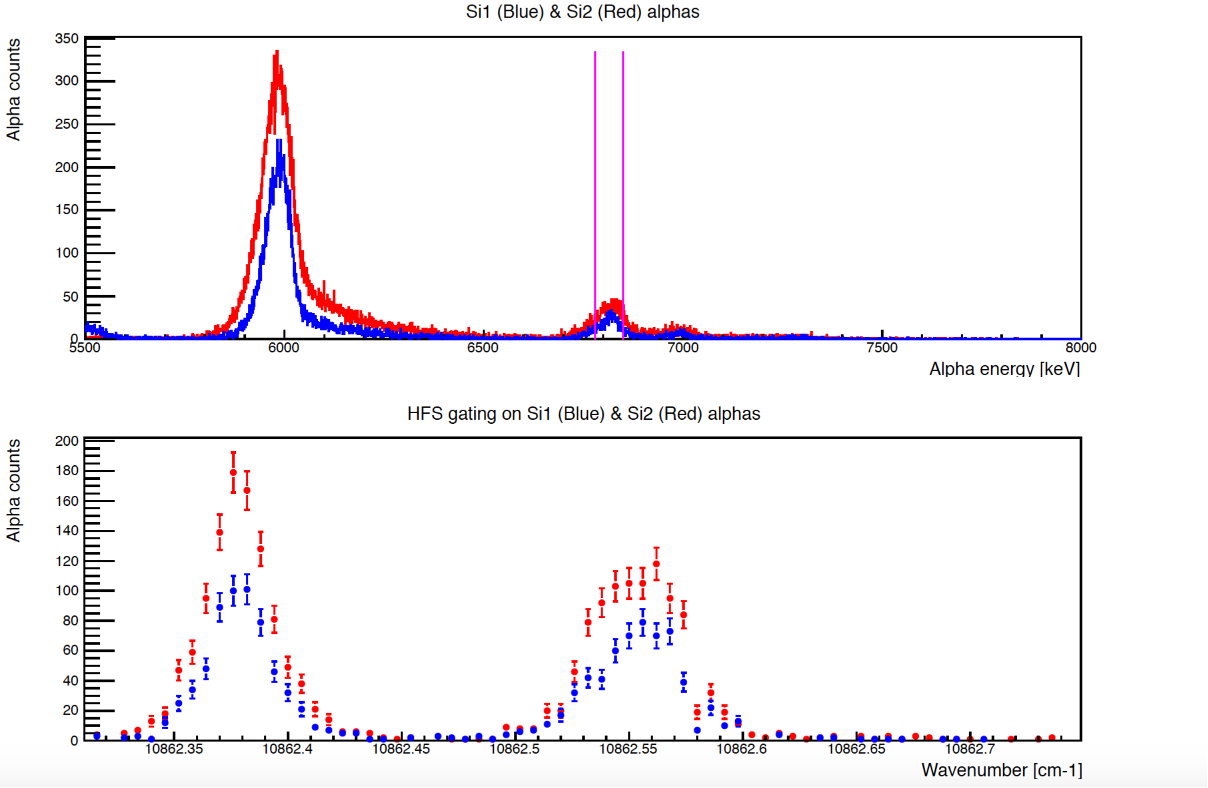

**Figure 4.30:** HFS plot for file 0219_0220 of $^{188}$Bi. Energy gate placed around the peak seen at 6813 keV (10- isomer), in order to produce the HFS present at the implantation site.

The HFS for file 0221_0222 can be seen in figure 4.31. This scan decreased in wavenumber from 10862.748591 cm$^{-1}$ to 10862.399647 cm$^{-1}$ with a run time of 12054 s, at 2 SC/step. In total there were 122 steps for this scan.

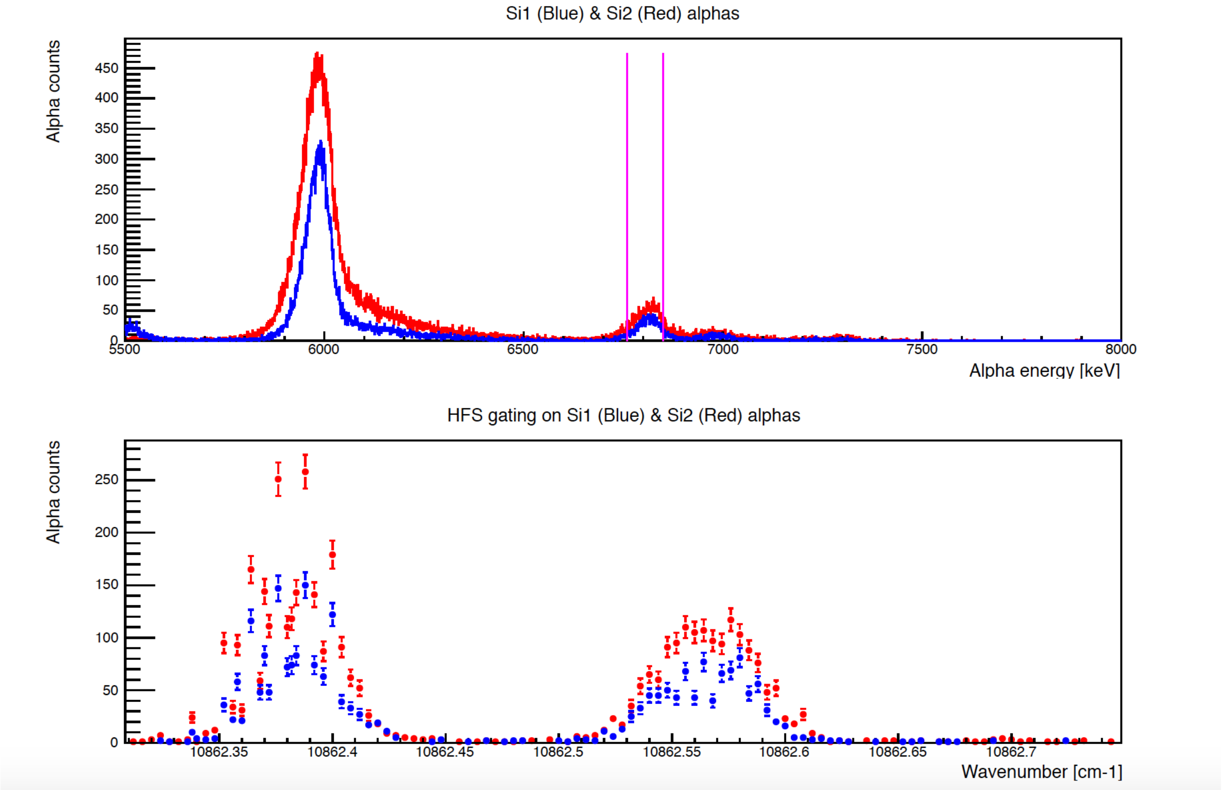

**Figure 4.31:** HFS plot for file 0221_0222 of $^{188}$Bi. Energy gate placed around the peak seen at 6813 keV (10-), in order to produce the HFS seen at the implantation site.

Overlap of HFS for the (3+) isomeric state decay seen in figure 4.32 and the (10-) ground state decays in figure 4.33.

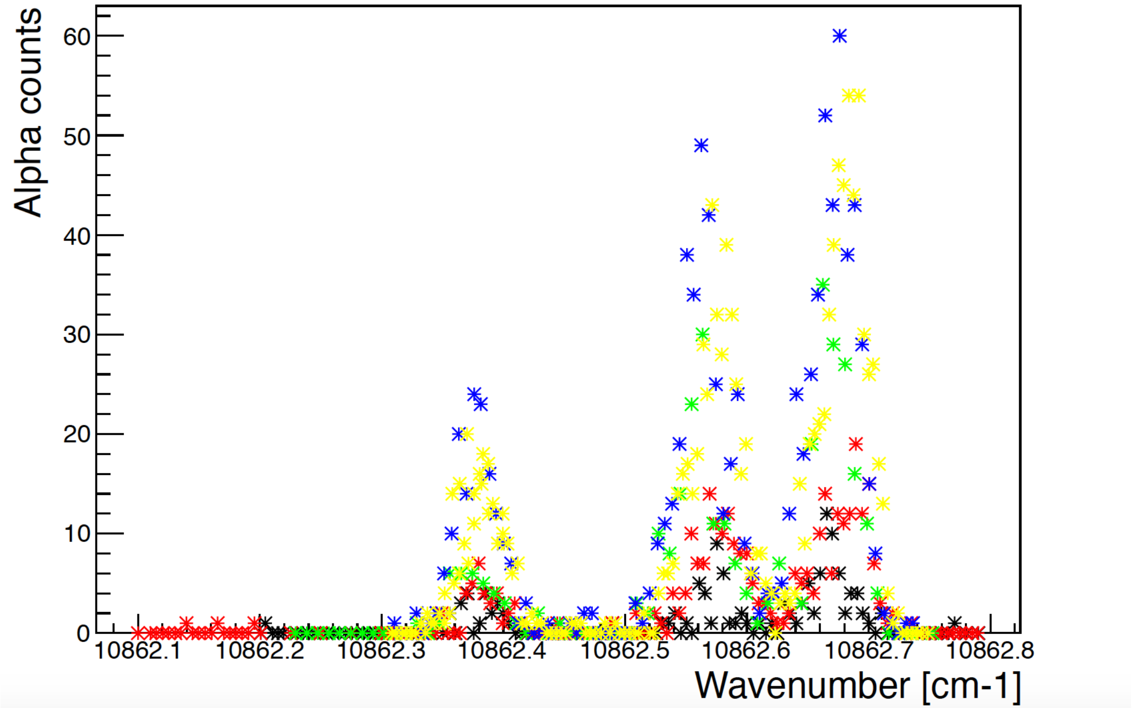

**Figure 4.32:** Overlap of the (3+) isomeric state decays HFS from all files during the $^{188}$Bi run. File 0158 (black points), file 0162_0163_0164 (red points), file 0162_0163_0164 (green points), file 0219_0220 (blue points) and file 0221_0222 (yellow points).

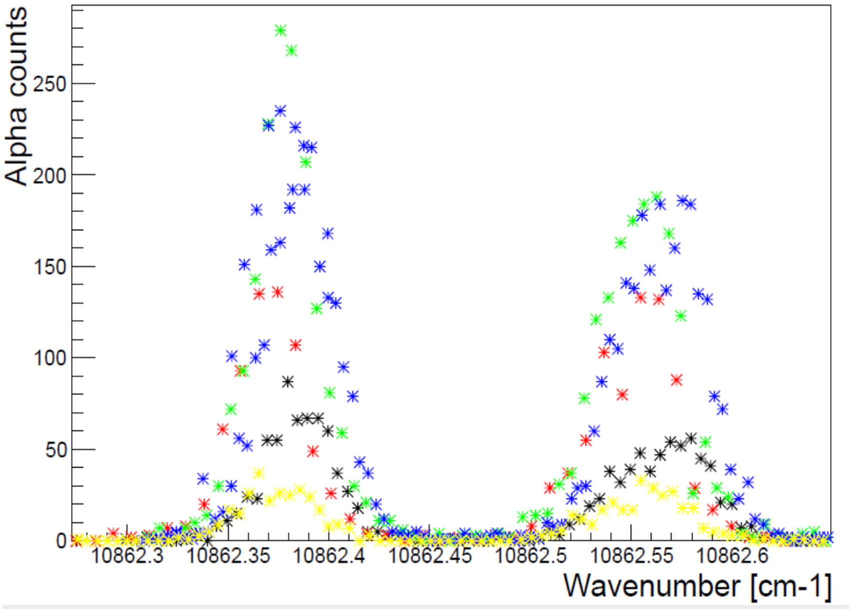

**Figure 4.33:** Overlap of the (10-) ground state decays HFS from all files during the $^{188}$Bi run. File 0158 (Yellow points), file 0162_0163_0164 (black points), file 0162_0163_0164 (red points), file 0219_0220 (green points) and file 0221_0222 (blue points).

## 4.4 $^{187}$Bi Analysis

During the $^{187}$Bi run, three scans took place; files 0170_0171, 0172_0173_0174_0175_0176 and 0177_0178_0179_0180_0181_0182. Figure 4.34 demonstrates that there are four possible $\alpha$ decays of two isomeric states in $^{187}$Bi. Statistics are low throughout the three scans done on $^{187}$Bi which leads to poor HFS spectra therefore, a larger alpha gate was used in order to increase the number of data points.

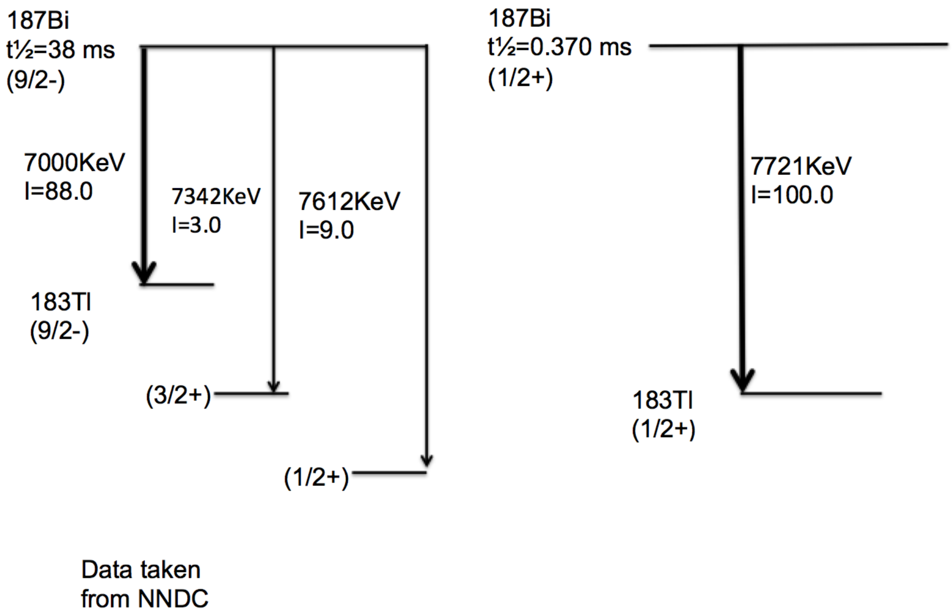

**Figure 4.34:** Decay scheme of $^{187}$Bi showing all possible alpha decays from both the ground and an isomeric state. Relative intensity (I) and half lives ($t_{1/2}$) given. Data taken from [4].

Only one alpha decay was detected at the implantation site for each scan of $^{187}$Bi. Figures 4.35, 4.36 and 4.37 show a peak seen at 7000 keV. This peak is a result of the alpha decay of the ground state (9/2-) of $^{187}$Bi to an isomeric state (9/2-) of $^{183}$Tl. Throughout the three scans of $^{187}$Bi two contaminants were present. At 5530 keV a high intensity $^{187}$Tl peak is seen, at both 6080 keV and 6190 keV a peak due to an alpha decay of $^{187}$Pb can also be observed.

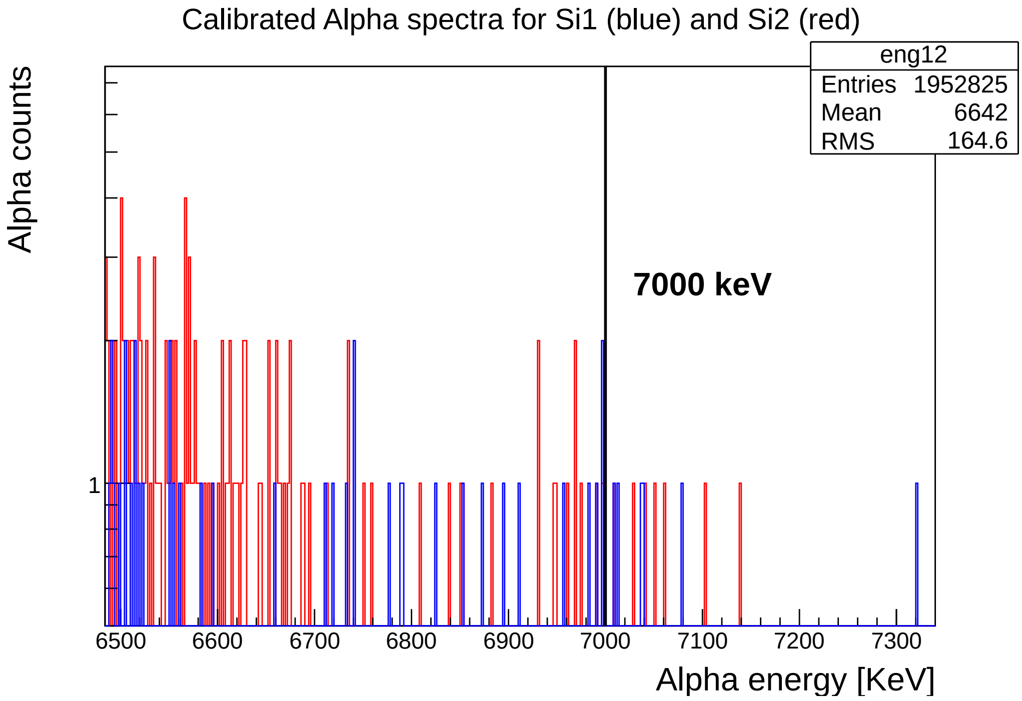

**Figure 4.35:** Alpha decay spectra from file 0170_0171 of $^{187}$Bi.

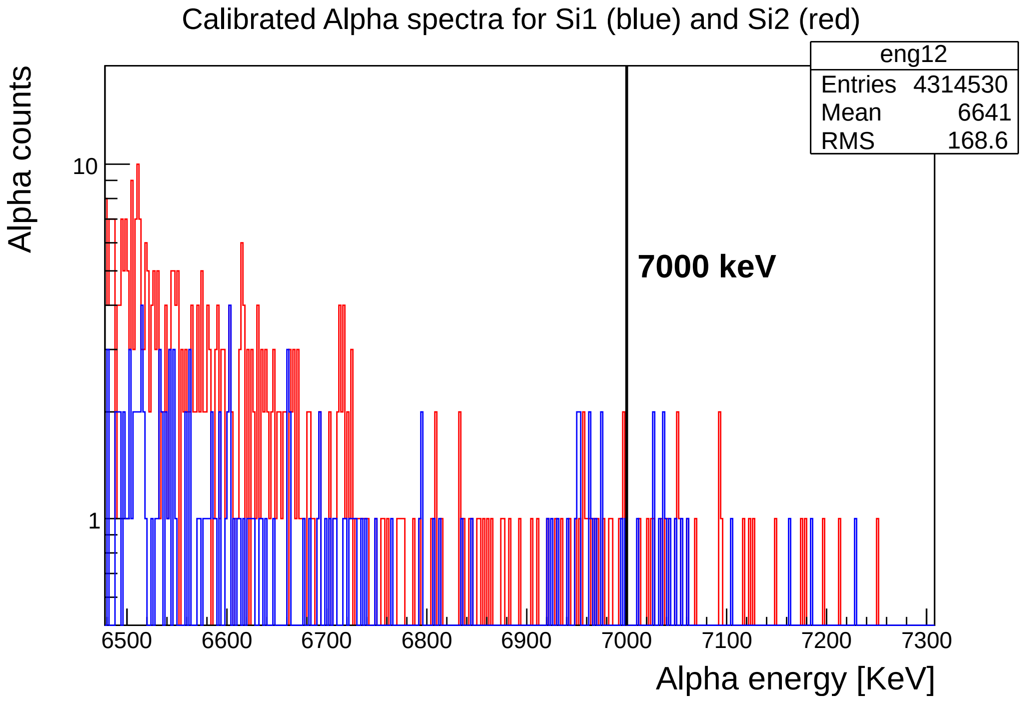

**Figure 4.36:** Alpha decay spectra from file 0172_0173_0174_0175_0176 of $^{187}$Bi.

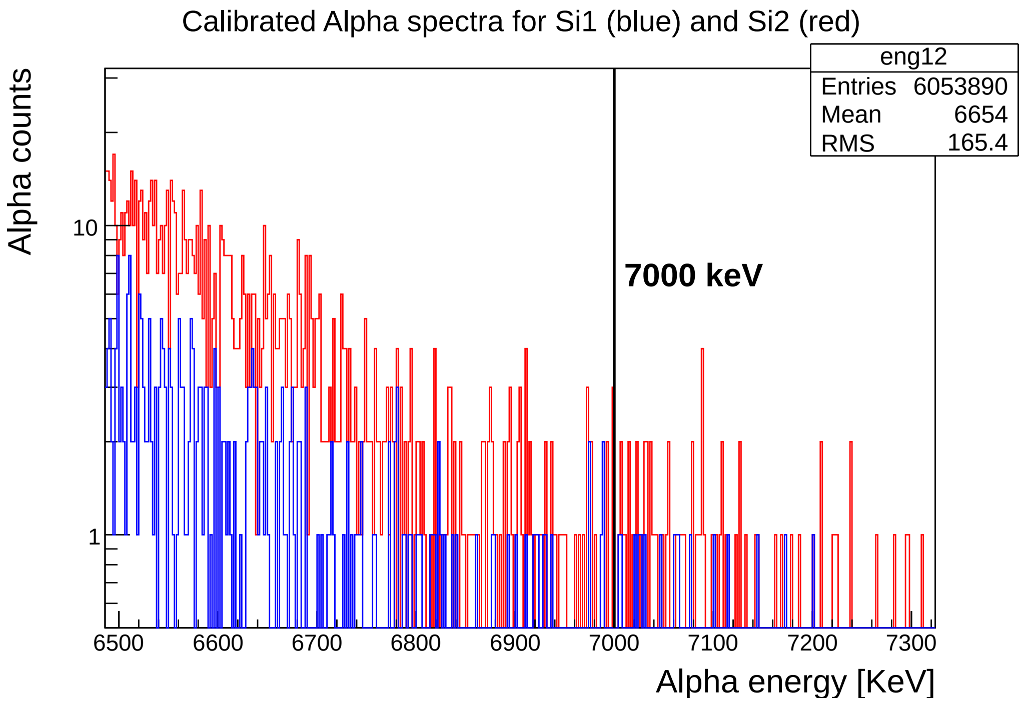

**Figure 4.37:** Alpha decay spectra from file 0177_0178_0179_0180_0181_0182 of $^{187}$Bi.

The peak detected at 7000 keV, the (9/2-) ground state decay, was gated from 6950 keV to 7050 keV, for file 0170_0171 yielding the HFS plot shown in the lower panel of figure 4.38. This scan increased in wavenumber from 10862.269627 cm$^{-1}$ to 10862.670591 cm$^{-1}$ with a run time of 4935.5 s, at 6 SC/step. In total there were 26 steps for this file. Figure 4.39 displays the laser power and proton current plots for file 0170_0171.

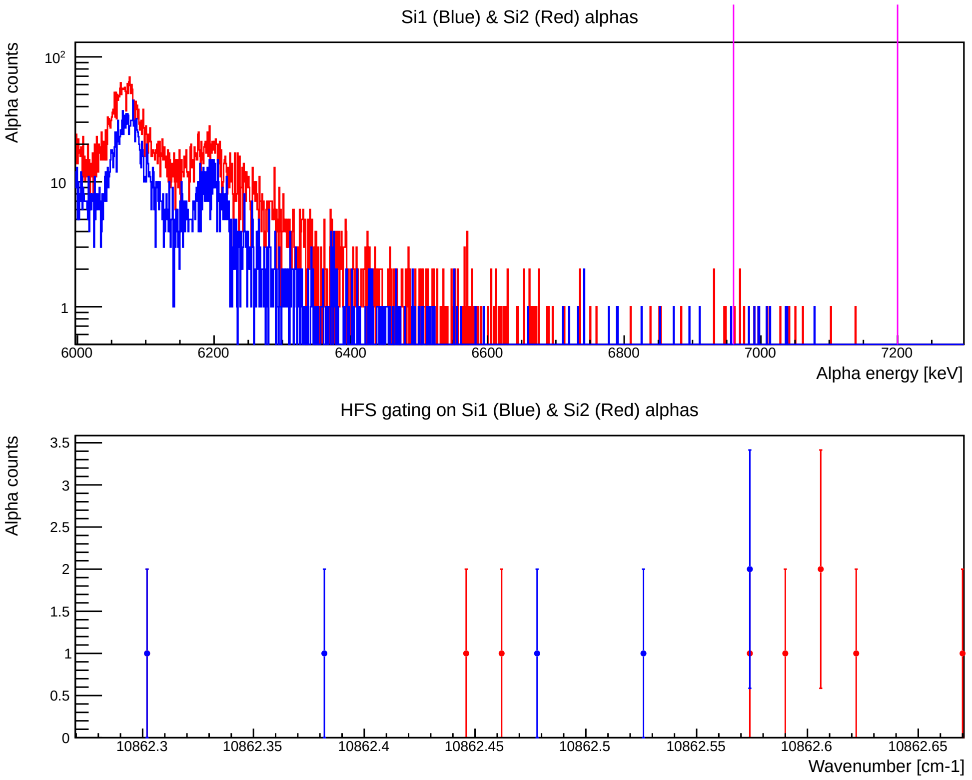

**Figure 4.38:** HFS plot for file 0170_0171 of $^{187}$Bi. Energy gate placed around the peak detected at 7000 keV (9/2- isomer), resulting in the production of HFS witnessed at the site of implantation.

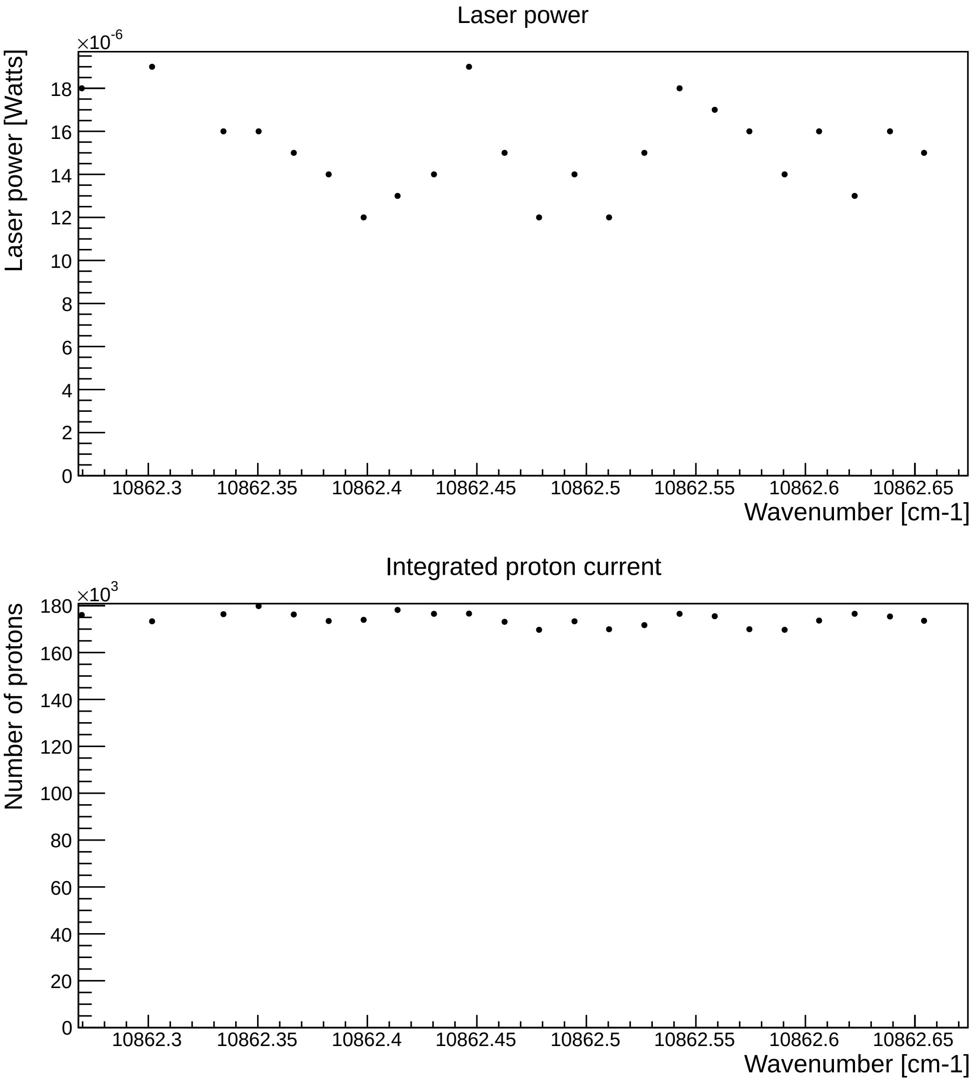

**Figure 4.39:** Laser power and proton current plots for file 0170_0171 of $^{187}$Bi.

The HFS for file 0172_0173_0174_0175_0176 can be seen in figure 4.40. This scan decreased in wavenumber from 10862.686367 cm$^{-1}$ to 10862.262385 cm$^{-1}$ with a run time of 8218 s, at 6 SC/step. In total there were 44 steps for this scan. The alpha gate remained the same as in file 0170_0171.

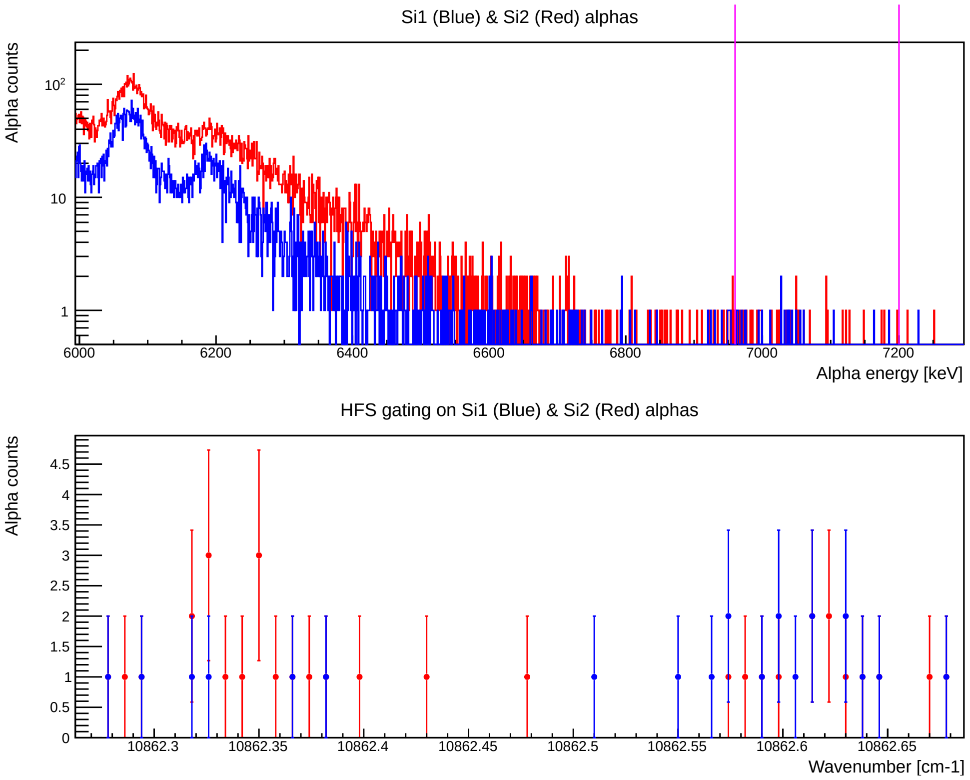

**Figure 4.40:** HFS plot for file 0172_0173_0174_0175_0176 of $^{187}$Bi.

The HFS for file 0177_0178_0179_0180_0181_0181 can be seen in figure 4.41. This scan increased in wavenumber from 10862.262371 cm$^{-1}$ to 10862.694434 cm$^{-1}$ with a run time of 8186 s, at 6 SC/step. In total there were 45 steps for this scan.

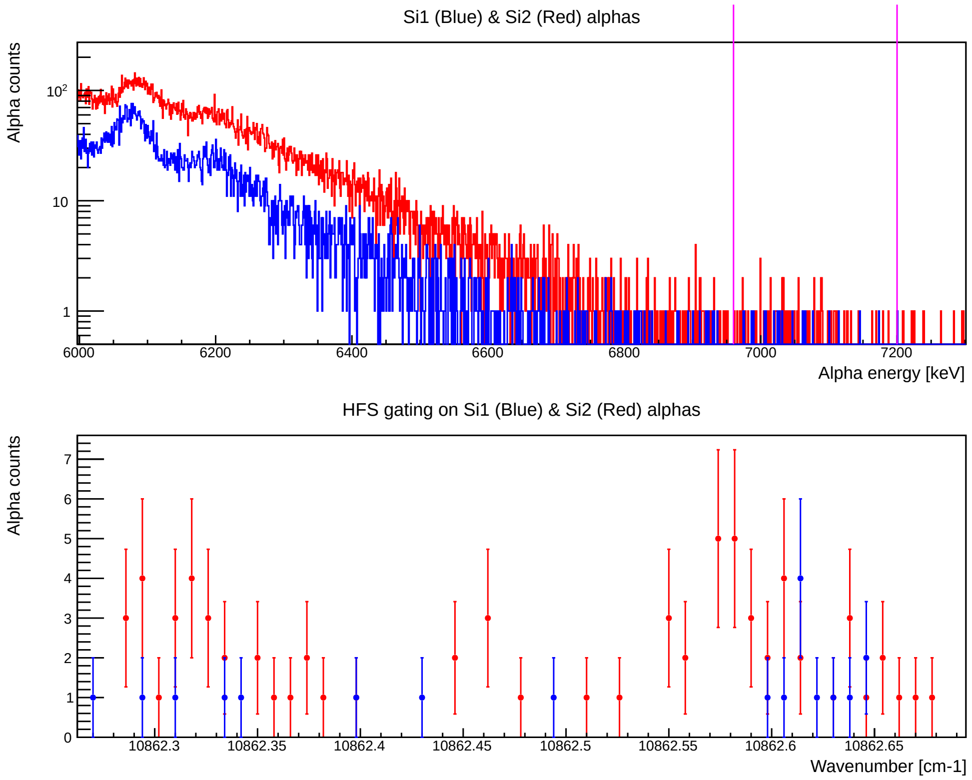

**Figure 4.41:** HFS plot for File 0177_0178_0179_0180_0181_0182 of $^{187}$Bi.

In figure 4.42 an overlap of ground state decays is provided. Due to the low statistics of this run the shape of HFS spectra is not as clear as the previous isotopes analysed however, two peaks are still present suggesting two allowed transitions with the HFS. This is not the case as stated in section 1.3, Doppler broadening and resolution of the detectors used cannot produce the individual peaks expected, resulting in multiple smaller peaks taken to be one larger.

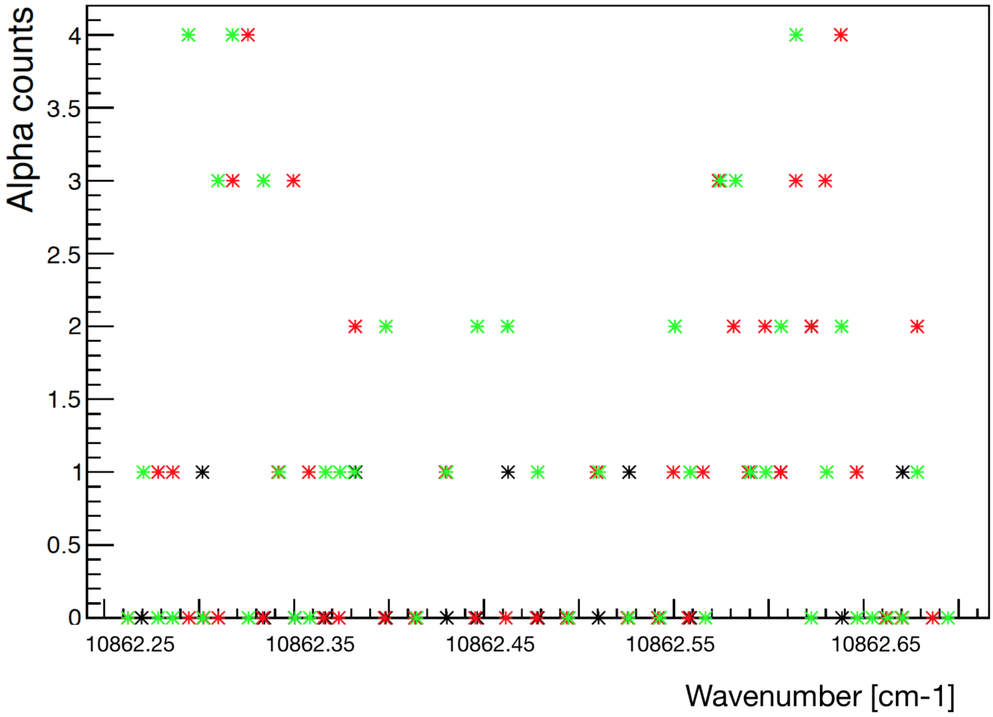

**Figure 4.42:** Overlap of the (9/2-) isomeric state decays HFS from all files during the $^{187}$Bi run. File 0170_0171 (black points), file 0172_0173_0174_0175_0176 (red points) and file 0177_0178_0179_0180_0181_0181 (green points).

# Chapter 5

# Discussion

## 5.1 Isotope shift

After all the data collected had been analysed a combined plot, seen in figure 5.1, was produced. The best (cleanest shape and with the most counts) HFS plot from each isotope was taken and lined up with the others so the isotope shift could easily be seen. Black lines were drawn through the centres of gravity of each peak in the plot of $^{191}$Bi, carrying on through to the bottom of $^{187}$Bi plot. $^{191}$Bi is used as a reference point from which the isotope shift can be calculated. The isotope shift calculated in this thesis, however, is only an estimation as correct fitting procedure must be done to determine the field shift hence, the isotope shift. Table 5.1 provides a summary of the centres of gravity of each isotope measured and the isomer shift for $^{191}$Bi and $^{188}$Bi. When referring to Table 5.1 note that a shift of the centre of gravity of 1.0 cm$^{-1}$ is equivalent to 30 GHz.

There is a reduction in wavenumber of 0.05 cm$^{-1}$ which is equivalent to 1.5 ±0.4 GHz between the centres of gravity of the ground states of $^{191}$Bi and $^{189}$Bi. The wavenumber continues to decrease as the centre of gravity in the HFS of $^{188}$Bi shifts a further 0.02 cm$^{-1}$ or 0.6 ±0.4 GHz from $^{189}$Bi. It is only when $^{187}$Bi has been reached that the centre of gravity increases with respect to the isotope before it, $^{188}$Bi. An increase of 0.04 cm$^{-1}$ or 1.2 ±0.4 GHz occurs. However there is still a decrease in wavenumber in comparison with $^{191}$Bi, a reduction of 0.03 cm$^{-1}$ or 0.9 ±0.4 GHz is seen.

With regards to the isomeric states, an increase in wavenumber of 0.11 cm$^{-1}$ or 3.3 ±0.4 GHz between $^{191}$Bi and $^{188}$Bi is present. From the isotope shift demonstrated in both an isomeric state and the ground, we can deduce that the size of the nucleus changes from isotope to isotope. Amongst the isotopes measured there is a large radii difference. A plot similar to the one seen in figure 2.1 which currently has unpublished data points, hence, cannot be used in this work, exhibits trends amongst a range of elements present in the neutron-deficient lead region. Data points for Bi follow the gradual sloping trend seen across all the other elements displayed in the plot, yet, comparable to Hg and Au a dramatic change in charge radii is seen when approaching the N=104 mid-shell region. For future work it would be beneficial to examine $^{186}$Bi to establish whether or not Bi will replicate the behaviour seen in Hg. Using the changes in charge radii one can estimate the shape of the nucleus.

**Table 5.1:** Summary of the Centres of Gravity of Bi isotopes Measured and Isomer Shifts.

| Bi Isotope | Centre of Gravity of Ground State ( cm$^{-1}$) | Centre of Gravity of Isomeric State ( cm$^{-1}$) | Isomeric Shift (GHz) |
|---|---|---|---|
| 191 | 10862.52 | 10862.54 | 0.6 |
| 189 | 10862.47 | - | - |
| 188 | 10862.45 | 10862.63 | 5.4 |
| 187 | 10862.49 | - | - |

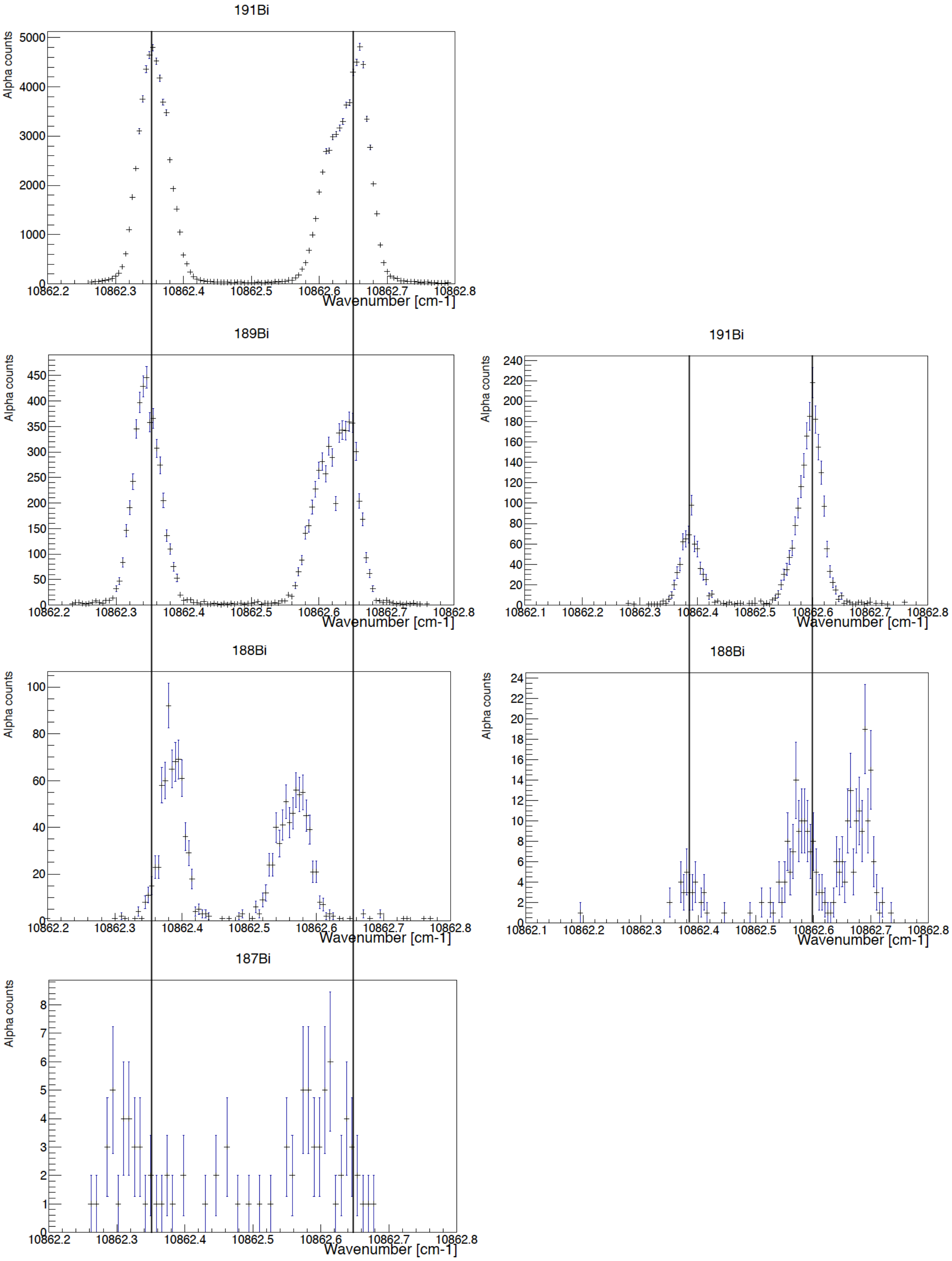

Ground state

Isomeric state

**Figure 5.1:** Plot to demonstrate isotope shift across all isotopes evaluated during this experiment. Isotope shift shown in both the ground state and an isomeric state. During this experimental run the presence of an isomeric state was only seen in $^{191}$Bi and $^{188}$Bi.

## 5.2 Isomer shift in $^{188}$Bi

Amongst all the isotopes of Bi studied during this experimental run, $^{188}$Bi demonstrates a considerable isomeric shift as seen in figure 5.2. The centre of gravity in the isomeric state (3+) is approximately 10862.63 cm$^{-1}$ and 10862.45 cm$^{-1}$ in the ground state (10-). A shift of 0.18 cm$^{-1}$ which is equivalent to 5.4 ±0.4 GHz is present. As previously mentioned there is another decay from an isomeric state of $^{188}$Bi to an isomeric state (3+) of $^{184}$Tl. This added data points to the (3+) HFS plot from the (10-) decay as the alpha gate contained both peaks. Hence, the centre of gravity for the (3+) state was calculated between the two right-hand peaks. Such a large isomer shift indicates a considerable difference in the radius of the nucleus from the ground state to a highly excited isomeric state.

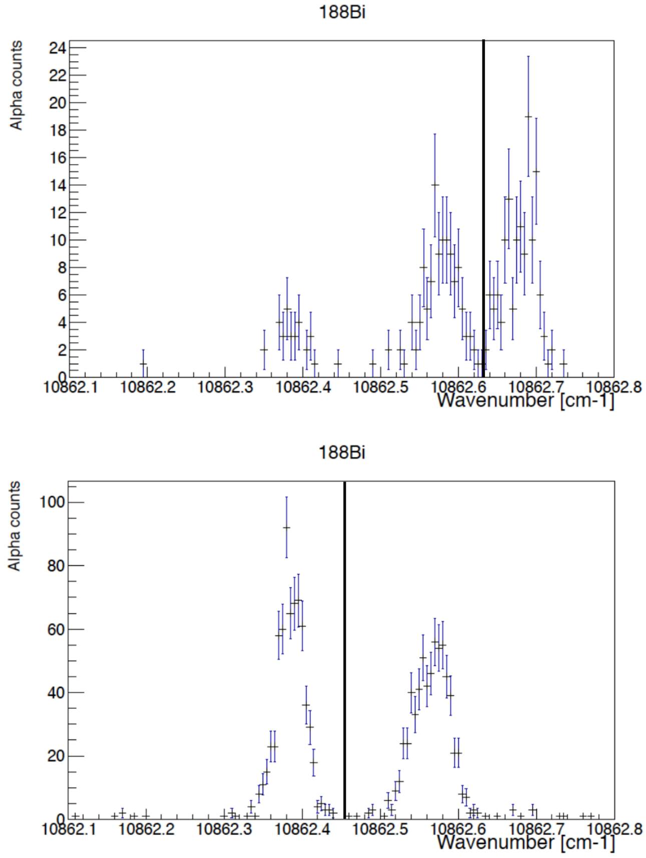

**Figure 5.2:** Isomer shift between the ground state and an isomeric state of $^{188}$Bi. The most prominent example of isomer shift seen in this experiment. The top panel is an isomeric state (3+) of $^{188}$Bi, the lower is the ground state (10-). Lines (black) have been drawn on each plot to clearly show the centres of gravity.

## 5.3 Shape coexistence

In theory, once the analysis shown in the previous chapter had been completed and values for the charge radii established, one can deduce the shape of the nucleus. Calculations cannot provide us with the shape of the nucleus, we can only find $\beta$, the deformation parameter, thus we can determine how much the nucleus deviates from a spherical shape. However, due to only using estimations for the isotope shifts in this work, plots have been taken from other sources to provide evidence of shape coexistence amongst the Bi isotopes studied. Figure 5.3 clearly displays a multitude of co-existing minima (near-spherical, oblate and prolate) amongst a range of Bi isotopes. Both $^{209}$Bi and $^{205}$Bi were not analysed in this work yet, are provided as a comparison.

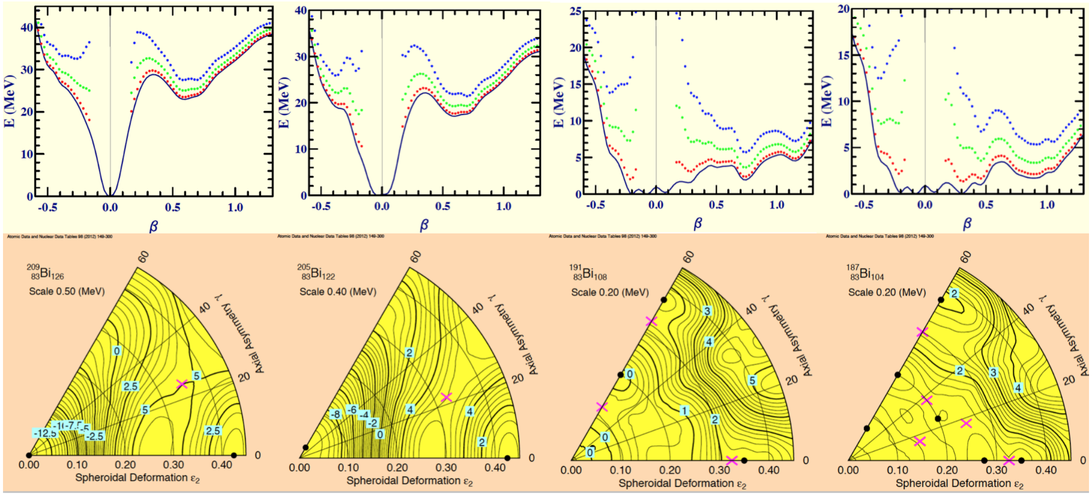

**Figure 5.3:** Energy surface plots demonstrating shape coexistence over multiple isotopes of Bi. Bottom row of figures taken from [35], top row of figures taken from [36]. From left to right, $^{209}$Bi, $^{205}$Bi, $^{191}$Bi and $^{187}$Bi. For the plots in the lower panel minima are indicated by the black dots and pink crossed lines for saddle points. Oblate nuclei have an axial symmetry ($\gamma$) of 60° whereas when $\gamma = 0°$ the nucleus is prolate. See text for a detailed explantation.

An initial look at all the plots shown in figure 5.3 indicates that as the neutron number decreases there is a gradual development of deformation of the nucleus. Starting with $^{209}$Bi the nucleus is spherical as demonstrated by the sharp and narrow minima, deformation begins to occur leading to the nucleus of $^{187}$Bi becoming very deformed. The top row of plots are Hartree-Fock calculations and are plotted as a function of $\beta$, the rotational energy correction for spins I= 8, 16 and 24 are indicated by the dashed lines. The bottom row are plots from P. Möller's calculations [35]. Energies used in both sets of plots will deviate as they are different models and are all relative. In $^{209}$Bi two minima are present, the clear dominant minima of the ground state seen at zero and a highly excited deformed state with a deformation of approximately 0.6. These minima can also be seen in the lower panel of figure 5.3, in the P. Möller's calculations. At E= -12.00 MeV there is a minima (a spherical nucleus) followed by another minima at E= 1.00 MeV, a prolate form of the nucleus, with a spheroidal deformation of 0.45. Minima with a higher energy represent an excited state, the greater the energy the greater the depth of the minima. Saddle points are shown by the pink crossed lines, a deformed saddle point is shown at E= 5.00 MeV, with a spheroidal deformation of 0.35. Deformation parameters used are different in both types of plot, however, $\beta$ can be derived from the spheroidal deformation.

Comparable to $^{209}$Bi, $^{205}$Bi displays two minima and one saddle point. From the Hartree-Fock calculations $^{205}$Bi is classed as a spherical nucleus, yet, exhibits some softness as deformation begins to take place with the decreasing neutron number. The highly excited deformed minima begins to decrease in energy in comparison with $^{209}$Bi. A minima of prolate nature is present at E= 0.8 MeV, $\epsilon_2$= 0.45, the spherical ground state is indicated by the minima at E= -9.6 MeV, $\epsilon_2$= 0.01. The one saddle point seen at E= 5.2 MeV, $\epsilon_2$= 0.32, represents a nucleus of a triaxial shape. Points with a deformation of 0.1 or lower are classed as spherical nuclei.

$^{191}$Bi demonstrates much different behaviour to the previous isotopes, unlike $^{209}$Bi and $^{205}$Bi there is no definitive shape, but a mix of oblate and prolate. A dramatic change is exhibited especially around $\beta$= 0, the result of multiple close lying minima is that the nucleus becomes very soft and broad in shape. Assessing the Hartree-Fock calculations suggests the nucleus will become oblate, by referring to the P. Möller plots this hypothesis is confirmed. It is clear that there is a large distribution of possibilities with regards to the shape of $^{191}$Bi nucleus. Three saddle points and four minima are present in $^{191}$Bi.

Once again $^{187}$Bi lacks any clear-cut shape due to a large number of minima and saddle points so nearby. With a total of six minima, five saddle points each of which varies in oblate and prolate nature, the nucleus shape is soft and without form.

To summarise the nucleus starts off spherical in Bi isotopes with a higher number of neutrons, as seen in $^{209}$Bi. Removing neutrons increases the deformation of the nucleus, leading to a soft and oblate shape displayed in $^{191}$Bi, continuing to remove neutrons results in an exceedingly deformed nucleus, such as $^{187}$Bi.

# Chapter 6

# Conclusion

The hyperfine structure parameters and isotope shifts have been measured for the neutron-deficient bismuth isotopes (A = 187,188, 189 and 191). The measurements were performed at ISOLDE based at CERN via the in-source resonance-ionisation spectroscopy technique and the KU-Leuven Windmill setup. The data collected during the IS608 part I run demonstrated an isotope shift across the four isotopes evaluated. As the neutron number, decreased the centre of gravity within the HFS spectra shifted down in wavenumber until $^{187}$Bi was reached, which deviates only slightly in comparison to $^{191}$Bi. Such behaviour is known as shape staggering, also seen in isotopes of Hg. Data gathered throughout the IS608 part II experiment will be of great importance in order to fully understand shape coexistence amongst Bi isotopes. To expand on current work and confirm our suspicions isotopes of Bi with a lower numbers of neutrons need to be analysed, for example, $^{186}$Bi.

# Bibliography

[1] A. E. Barzakh et al. Onset of deformation in neutron-deficient Bi isotopes studied by laser spectroscopy. *Physical Review C*, 95:044324, 2017.

[2] Kenneth S. Krane. *Introductory Nuclear Physics.* John Wiley & Sons, 1988.

[3] K. Heyde. *Basic Ideas And Concepts In Nuclear Physics.* IOP Publishing Ltd, 1999.

[4] Brookhaven National Laboratory. National nuclear data centre. `https://www.nndc.bnl.gov`, July 2017.

[5] J.H.D. Jensen O. Haxel and H.E. Suess. On the ”magic numbers” in nuclear structure. *Physical Review*, 75:1766, 1949.

[6] R. F. Casten. *Nuclear Structure From A Simple Perspective.* Oxford University Press, 1990.

[7] Hyper Physics. Shell Model of Nucleus. `http://hyperphysics.phy-astr.gsu.edu/hbase/Nuclear/shell.html`.

[8] Douglas C.Giancoli. *Physics For Scientists And Engineers With Modern Physics.* Prentice Hall, 1988.

[9] Samuel S. M. Wong. *Introductory Nuclear Physics.* Wiley-VCH, 2004.

[10] Alexander Belyaev. Alpha Decay. `https://sites.google.com/site/alexandersbelyaev/teaching/phys3002`, .

[11] Hyper Physics. Electron Capture. `http://hyperphysics.phy-astr.gsu.edu/hbase/Nuclear/radact2.html`.

[12] Alexander Belyaev. Gamma Decay. `https://sites.google.com/site/alexandersbelyaev/teaching/phys3002`, .

[13] B. Cheal and K. T. Flanagan. Progress in laser spectroscopy at radioactive ion beam facilities. *JPhysG: Nuclear and Particle Physics*, 37:11, 2010.

[14] Ernst W. Otten. Nuclear Radii and Moments of Unstable Isotopes. *Treatise on Heavy Ion Science*, pages 517–638, 1989.

[15] P. Campbell, I.D. Moore, M.R. Pearson. Laser spectroscopy for nuclear structure physics. *Progress in Particle and Nuclear Physics*, 86:127–180, 2016.

[16] W. H. King. *Isotope Shifts in Atomic Spectra.* Plenum Press, 1984.

[17] A.R. Bodmer. Nuclear Scattering of Electrons and Isotope Shift. *Proceeding of the Physical Society. A*, 66:1041, 1953.

[18] H. Morinaga. Interpretation of Some of the Excited States of 4n Self-Conjugate Nuclei. *Physical Review*, 101:254–258, 1956.

[19] J. Bonn et al. Sudden change in the nuclear charge distribution of very light mercury isotopes. *Physics Letters B*, 38:308–311, 1972.

[20] A. Andreyev. Charge radii plot. Email.

[21] J. Kluge A. Andreyev. Exotic lead nuclei get into shape at ISOLDE. *CERN Courier*, pages 19–21, October 2007.

[22] D. Fedorov et al. T. Day Goodacre. Laser resonance ionization scheme development for tellurium and germanium at the dual Ti:Sa Dye ISOLDE RILIS. *Nuclear Instruments and Methods in Physics Research A*, 830:510–514, 2016.

[23] Erich Kugler. The ISOLDE Facility. *Hyperfine Interactions*, 129:23–42, 2000.

[24] A. Marsh, B. Andel et al. New developments of the in-source spectroscopy method at RILIS/ISOLDE. *Nuclear Instruments and Methods in Physics Research B*, 317:550–556, 2013.

[25] ISOLTRAP. High Precision Mass Measurements with the Penning Trap Mass Spectrometer ISOLTRAP at ISOLDE. `http://www-ap.gsi.de/research/posters/isoltrap/`.

[26] V. Fedosseev et al. Ion beam production and study of radioactive isotopes with the laser ion source at ISOLDE. *Journal of Physics G: Nuclear and Particle Physics*, 44, 2017.

[27] H. De Witte et al. Alpha-decay of neutron-deficient 200Fr and heavier neighbours. *The European Physical Journal A*, 23:243–247.

[28] A.N. Andreyev, J. Elsviers et al. New Type of Asymmetric Fission in Proton-Rich Nuclei. *Physical Review Letters*, 105:252502, 2010.

[29] R. N. Wolf, et al. A multi-reflection time-of-flight mass separator for isobaric purification of radioactive ion beams. *Hyperfine Interact*, 199:115–122, 2011.

[30] F. Wienholtz et al. Masses of exotic calcium isotopes pin down nuclear forces. *Nature*, 498:346–349, 2013.

[31] A.N. Andreyev, et al. Shape-coexistence and shape-evolution studies for bismuth isotopes by in- source laser spectroscopy and beta-delayed fission in 188Bi. *European Organization For Nuclear Research*, Proposal to ISOLDE and Neutron Time-of-Flight Committee, 2015.

[32] CERN. ISOLDE Decay Station (IDS). `http://isolde.web.cern.ch/experiments/isolde-decay-station-ids`.

[33] IDS. ISOLDE Decay Station (IDS) website, Detection set-up. `http://isolde-ids.web.cern.ch/isolde-ids/`.

[34] Oliver S. Kirseboom Hans Fynbo and Olof Tengblad. ISOLDE decay station for decay studies of interest in astrophysics and exotic nuclei. *JPhysG: Nuclear and Particle Physics*, 44:5, 2017.

[35] P. Moller et al. Nuclear shape isomers. *Atomic Data and Nuclear Data Tables*, 98:149–300, 2012.

[36] The French Alternative Energies and Atomic Energy Commission (CEA). Potential energy surface for Bismuth. `http://www-phynu.cea.fr/science_en_ligne/carte_potentiels_microscopiques/noyaux/zz83/sep/zz83n104sep_eng.html`.